

Active metasurfaces: lighting the path to commercial success

Tian Gu^{1,2,*}, Hyun Jung Kim^{3,4,*}, Clara Rivero-Baleine^{5,*}, and Juejun Hu^{1,2,*}

¹*Department of Materials Science & Engineering, Massachusetts Institute of Technology, Cambridge, Massachusetts, USA*

²*Materials Research Laboratory, Massachusetts Institute of Technology, Cambridge, Massachusetts, USA*

³*National Institute of Aerospace, Hampton, Virginia, USA*

⁴*NASA Langley Research Center, Hampton, Virginia, USA*

⁵*Missiles and Fire Control, Lockheed Martin Corporation, Orlando, Florida, USA*

**gutian@mit.edu, hyunjung.kim@nasa.gov, clara.rivero-baleine@lmco.com, hujuejun@mit.edu*

Abstract

Active optical metasurfaces are rapidly emerging as a major frontier in photonics research, development, and commercialization. They promise compact, light-weight, and energy-efficient reconfigurable optical systems with unprecedented performance and functions that can be dynamically defined on-demand. Compared to their passive counterparts, the reconfiguration capacity of active metasurfaces also set additional challenges in scalable design, manufacturing, and control toward their practical deployment. This perspective aims to review the state-of-the-art of active metasurface technologies and their applications while highlighting key research advances essential to enabling their transition from laboratory curiosity to commercial reality.

Main

Optical metasurfaces are artificial media comprising planar arrays of sub-wavelength structures (commonly called meta-atoms). With their now well-recognized advantages in optical performances, form factor and cost, metasurfaces are witnessing a move toward commercial adoption: a solid lineup of large corporations as well as a cohort of aspiring start-up companies are heavily investing on R&D in this field.

Active metasurfaces introduce a new dimension to the space, enabling dynamic tuning of optical functions while promising wide-ranging applications in analog computing¹, data communications², optical camouflage³, reconfigurable imaging⁴, light detection and ranging (LiDAR)⁵, display⁶, imaging spectroscopy⁷, nonreciprocal photonics⁸, and many others. As the interest in active metasurfaces percolates from academia to industry, important questions arise regarding when and how their transition from lab to market will flourish. To address such questions, this perspective provides a bird's eye view on current state-of-the-art of active optical metasurface technologies, surveys emerging applications capitalizing on their unique attributes, and scrutinizes the technological gaps that need to be filled to transform the prospective applications into reality.

The present state-of-the-art in active metasurface technologies

Active tuning schemes of metasurfaces can in general be classified into two categories, one where the optical responses of the meta-atoms are modified and the other relying on mechanical movement of meta-atoms. The former scheme usually involves modulating the optical properties of the meta-atoms or their surrounding material, for instance via free carrier injection⁹, Pockels effect¹⁰, quantum confined Stark effect¹¹, thermo-optic coupling¹², electrochromism¹³, magneto-optical interaction¹⁴, and structural transitions in various materials^{15–17}, whereas the latter can leverage either macroscopic displacement¹⁸/deformation¹⁹ or micro-electromechanical system (MEMS) actuation²⁰. State-of-the-art performances of these tuning mechanisms as well as their respective fundamental limits in optical loss, speed, and endurance are summarized in Table 1.

Besides key performance attributes defined by optical contrast, loss, speed, endurance and volatility, the likelihood of an active metasurface technology to enter mainstream adoption in the near- or mid-term is largely dictated by its technology and manufacturing readiness levels (TRL and MRL). From this technology maturity perspective, liquid crystal (LC) and MEMS based metasurfaces are among the most established candidates, as both make use of proven industry-standard technologies to introduce active tuning capabilities and can also take advantage of an established industrial ecosystem to facilitate high-volume device manufacturing and packaging. Other promising contenders involve new materials such as transparent conducting oxides (TCOs) and chalcogenide phase change materials (PCMs). Even though these materials are not part of the standard offerings of most silicon foundries today, they are readily amenable to foundry-compatible backend integration: TCOs constitute an integral element of modern-day display panel production process and PCMs have already become a key ingredient in commercial nonvolatile memories. Integration of these new materials and metasurface architectures into mainstream manufacturing processes will be motivated by practical application demands as discussed in the succeeding section.

Application prospects: where they will shine

Before delving into the applications of active metasurfaces, one should be reminded that actively tunable optics is not a new concept. Technologies exemplified by adaptive optics harnessing deformable mirrors for real-time wavefront correction in astronomical telescopes and spatial light

modulators (SLMs) building on digital light processing or liquid crystal on silicon (LCoS) have been meticulously perfected over the past decades. So, what do active metasurfaces have to offer?

Their drastically reduced Size, Weight and Power (SWaP) characteristics promise reconfigurable optical systems that are ultracompact, light-weight, energy-efficient and rugged. Their optically-thin, pixelated device architecture further enables fast tuning mechanisms not compatible with conventional bulk optics. Space applications represents one of the emerging arenas where these characteristics are highly prized (Box 1). Moreover, such size down-scaling does not come with the usual penalties of compromised optical quality or lack of fine control, thereby setting active metasurfaces apart from other competing tunable micro-optics technologies relying on electrowetting, liquid metals, and soft elastomeric optics. Active metasurfaces are thus also well poised for applications such as augmented/virtual reality (AR/VR) and point-of-care or minimally invasive biomedical imaging, where form factor and optical precision are equally critical.

Another defining character of active metasurfaces is their capacity for on-demand wavefront manipulation down to the sub-wavelength scale. This unprecedented granularity permits light bending at extreme angles that traditional refractive or diffractive optics cannot accommodate while effectively suppressing spurious diffraction orders^{21–23}. Beam steering devices with high efficiency and large field-of-view (FOV) can be created capitalizing on this feature (Box 2). The agile beam control capability, coupled with high spatial density afforded by metasurface optics, potentially envisions glasses-free 3-D displays offering high resolution, large viewing angle, and full color coverage (Box 3). Finally, the ability to engineer a metasurface’s phase profile in an almost arbitrary manner proves valuable to computational imaging and sensing, since the transfer function of the frontend meta-optics can be co-designed holistically with the backend processing algorithm to enhance signal extraction and maximize the signal-to-noise ratio²⁴. It has been shown that active meta-optics designed using such an approach can yield *optimal* imaging systems capable of multi-dimensional (spatial, spectral, polarization, light field, etc.) information retrieval²⁵.

Finally, since many active metasurfaces are produced using semiconductor nanofabrication technologies, they can be seamlessly integrated with semiconductor electronic and photonic devices to create ‘metasurface-augmented’ optoelectronics with novel functionalities, whereas such wafer-level integration is often challenging or impractical for conventional tunable micro-optics.

These unique advantages presented by active metasurfaces foreshadow an array of potential applications outlined in Table 2. The key takeaway message is that there is no “one-size-fits-all” solution, because each application prioritizes a different set of performance metrics that none of the active metasurface technologies today (Table 1) can simultaneously meet. Table 2 also distinguishes two types of tuning schemes: discrete and continuous. In the former case, the metasurface only accesses a small number of optical states, and such discrete tuning over multiple arbitrary phase profiles can be accomplished by collective switching of all meta-atoms across the aperture²⁶. On the other hand, it is generally believed that continuous tuning, where a large number or a continuum of states are mandated, necessitates independent control of individual or small groups of meta-atoms. In the following section, we will propose a new concept defying this conventional wisdom to achieve continuous tuning with a much simplified switching fabric. Other research challenges that need to be addressed to fulfill the application demands will also be elaborated.

Box 1. Active metasurfaces in aerospace applications

The growth in aerospace systems has been underpinned by increasing capabilities being packed into smaller and lighter spacecrafts, which requires robust, light-weight components to deliver enhanced science data products while constrained by lean SWaP budgets. Future growth in the capabilities of earth observation, deep space, and planetary surface missions using miniaturized spacecraft platforms can only be sustained by innovations in the design of remote sensors and other sub-systems. Enhanced tunability and reconfigurability empowered by active metasurface optics will be game changers for aerospace remote sensing applications, from LiDAR to new imagers, detectors and sensors. Active metasurface topics of interest to aerospace remote sensing include:

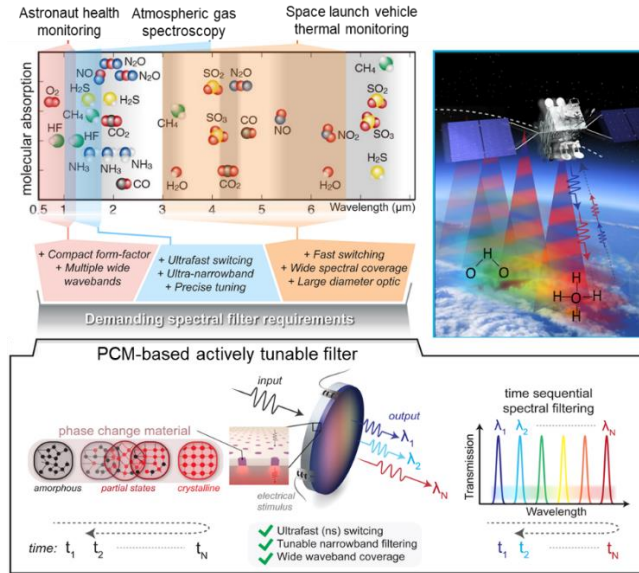
- ✓ beam shaping for antennae (optical and microwave wavelengths),
- ✓ reconfigurable (real-time phase-corrective) lenses and planar adaptive optics for imaging, optical communications, and high-gain antennae,
- ✓ beam steering for radar and LiDAR scanning systems, flat panels, and mobile communication antennae (optical, microwaves and millimeter-wave wavelengths), and
- ✓ tunable filter and spatial light modulators for imaging spectroscopy.

As an example, exoplanet imaging in space requires real-time wavefront corrections to mitigate the effects of thermal gradients, optical imperfections, and diffraction issues. An active exoplanet imaging mission at present is the James Webb Space Telescope, which is equipped with a sophisticated NIRCarn having several coronagraphs for imaging in the infrared. Active metasurface optics could lead to a space-based correction system with major SWaP advantages. This would permit characterization of the light from an exoplanet and even allow direct imaging of the planet via active cancelation of high frequency spatial and temporal aberrations.

Another application that active metasurfaces are poised to transform is multispectral imaging. Recently, PCM-integrated tunable optical filters have shown promise as multifunctional wide-band replacements for bulky filter wheels in spaceborne remote sensing sub-systems^{7,27,28}. This is achieved through the integration of PCM into a plasmonic nanohole metasurface to effectively tune the transmission passband of optical filters in real time. The solid-state metasurface filter is fast, have no moving parts, and does not require continuous input power to maintain the filter characteristics. Their applications include astronaut health monitoring, atmospheric gas sensing, and space launch vehicle thermal imaging as summarized conceptually in the figure.

As a specific use scenario, consider a tunable filter integrated remote temperature measurement system to collect calibrated multispectral images of air/spacecraft during ascent in order to validate the thermal protection systems of the vehicles. To make these measurements, state-of-the-art systems rely on motorized filter wheels which hold several (typically ~ 5) single-notch optical filters and rotate between filters to take new spectral measurements. The filter wheels offer no real-time tunability and are limited in overall bandwidth and temporal resolution, therefore missing out on important spectral and temporal data. In contrast, PCM-based active metasurface filters can be tuned within microseconds, enabling real-time thermography and imaging spectroscopy with high data throughput. Furthermore, LiDAR missions utilize the same filter wheels for chemical remote sensing. The broad waveband and robust tuning applicability of the PCM-based tunable filter provide unprecedented views of earth's atmospheric constituents and surface altimetry, significantly advancing science objectives across multiple disciplines. These features, in addition to the orders-of-magnitude

reduction in total SWaP, envisage that spaceborne systems incorporating PCM-based actively tunable filters will continue to be in demand into the foreseeable future.



(Top-left) Characteristic absorption bands of molecules of interest to aerospace applications as well as application-specific requirements on the tunable spectral filter; (top-right) satellite-based multispectral imaging for monitoring of atmospheric gas species; (bottom) operating principle of the PCM-based metasurface filter: the PCM's structure can be continuously tuned in a non-volatile manner via voltage pulses, thereby spectrally shifting the passband of the metasurface.

Box 2. Active metasurfaces for beam steering

Optical beam steering devices are gaining importance by the day with prospective applications in LiDAR for autonomous vehicles, remote sensing, and displays in AR/VR modules. A common embodiment of metasurface-based beam steering is to use the metasurface as an optical phased array (OPA). For normal incident input beam with wavelength λ , the deflection angle θ of the beam exiting from the metasurface OPA is given by:

$$\frac{2\pi}{\lambda} \cdot \sin \theta = \frac{\Delta\varphi \pm m \cdot 2\pi}{\Lambda}$$

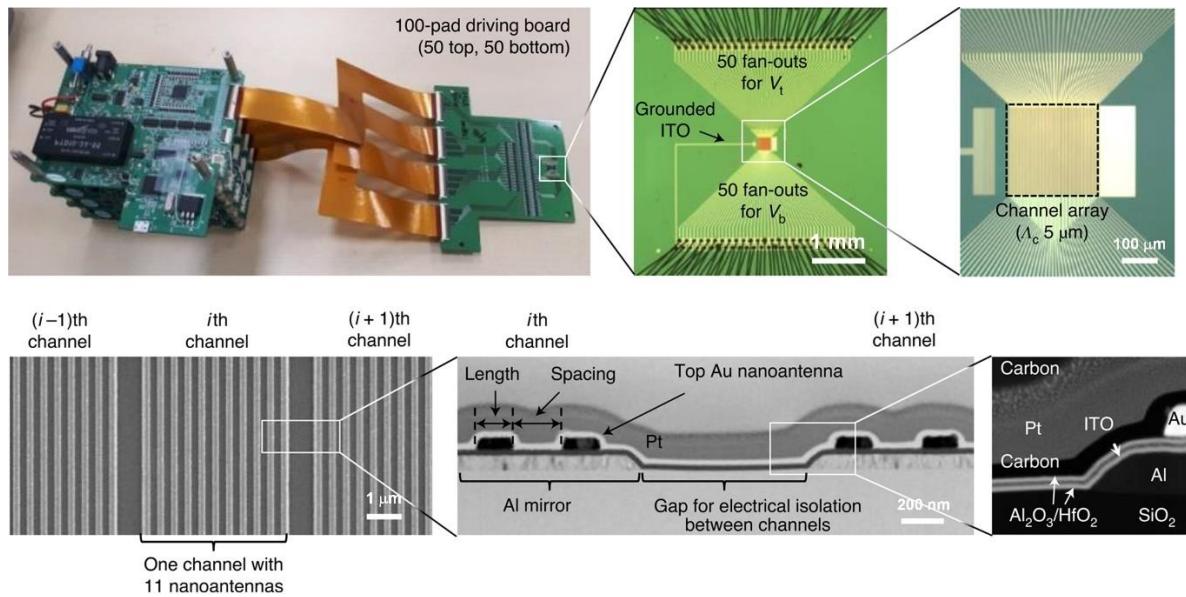
where Λ is the meta-atom pitch, $\Delta\varphi$ gives the phase delay between two neighboring meta-atoms ($0 \leq \Delta\varphi < 2\pi$), and m denotes the aliasing order. Ideally, the equation should only be satisfied when $m = 0$, thereby yielding a single solution of θ to eliminate aliasing. In an OPA with a FOV covering $-\theta_{\max}$ to θ_{\max} , this condition becomes:

$$\Lambda = \frac{\lambda}{2 \sin \theta_{\max}}$$

to ensure solution uniqueness. A small pitch Λ is therefore instrumental to suppressing aliasing and increasing FOV, a unique advantage of metasurfaces over their classical diffractive counterpart. Another benefit of a small pitch is that the wavefront can be more precisely sculpted at a deep sub-wavelength scale, thereby enhancing optical efficiency²⁹. This is particularly important for wide-FOV beam steering at large angles, where the wavefront follows a rapid spatial variation.

Besides aliasing suppression and FOV, the main performance requirements for beam steering devices include beam divergence (which relates to angular resolution), speed, and reliability. Beam divergence is specified by the optical aperture size, the number of meta-atoms and hence complexity of active control, while speed and reliability relate to the metasurface tuning mechanism. For automotive applications, an angular resolution of 0.2° or better is necessary, which translates to an aperture size of $\sim 200 \mu\text{m}$ or larger for near-IR LiDAR. Automotive applications further specify a baseline frame rate of 10 Hz (or higher), a typical combined (horizontal) FOV of 120° , and compliance with reliability standards set forth by IEC, ISO, ASTM and individual auto manufacturers, which mandate tolerance against temperature excursions, mechanical shock, vibrations, fatigue, dust, and salt mist. The reduced temperature sensitivity (as compared to traditional refractive optics) and structural ruggedness of metasurfaces present an additional edge.

Several active metasurface prototypes for beam steering have been demonstrated. Li *et al.* demonstrated a 1-D phase-only SLM based on a LC-infiltrated TiO_2 Huygens metasurface with an aperture size of $120 \mu\text{m} \times 100 \mu\text{m}$ ³⁰. Each electrically addressed pixel comprise three rows of meta-atoms with a combined width of $\sim 1 \mu\text{m}$. The device achieves a deflection efficiency of 36% at 660 nm wavelength and a FOV of 22° . In parallel, Lumotive, a start-up focusing on LiDAR technologies, has been developing a “Meta-LiDAR” platform based on LCoS³¹. While details of the technology are not available in the public domain, their patents describe LC-infiltrated metal antenna arrays as the active beam steering element.



(Top left) Active metasurface array mounted on an electronics board capable of independently driving 50 channels (pixels) with a pitch of $\Lambda_c = 5 \mu\text{m}$; (top right) optical microscopy images of the array; (bottom left) scanning electron microscopy image showing the 1-D pixels, each consisting of 11 meta-grating lines; (bottom right) transmission electron microscopy images showing cross-sectional structures of the active array⁵.

Beam steering at higher speed warrants alternative mechanisms. As illustrated in the figure, researchers from Samsung demonstrated active 1-D meta-gratings made of indium tin oxide (ITO), where each individually contacted pixel contains 11 grating lines⁵. A dual gate configuration was employed to realize independent control of phase and amplitude, a useful feature enabling apodization and sidelobe suppression. An RC-limited 3-dB bandwidth of 170

kHz was attained in a $200\text{ }\mu\text{m} \times 200\text{ }\mu\text{m}$ device with a FOV of 15.4° and a deflection efficiency between 34% to 48%. 2-D beam steering based on a similar mechanism was also reported recently³².

Before these pioneering demonstrations can enter the commercial realm, considerable performance improvements are anticipated. Down scaling the pixel size to the single meta-atom level will fully leverage the promised advantages of metasurface OPAs such as aliasing-free operation, high efficiency and large FOV. Angle-dependent and nonlocal metasurface designs will further enhance the performance of such large-angle meta-optical systems. A scalable electrical addressing scheme commensurate with large aperture active tuning is sought after to enhance resolution and facilitate agile 2-D beam steering. Finally, reliable packaging suitable for field deployment must be developed and validated.

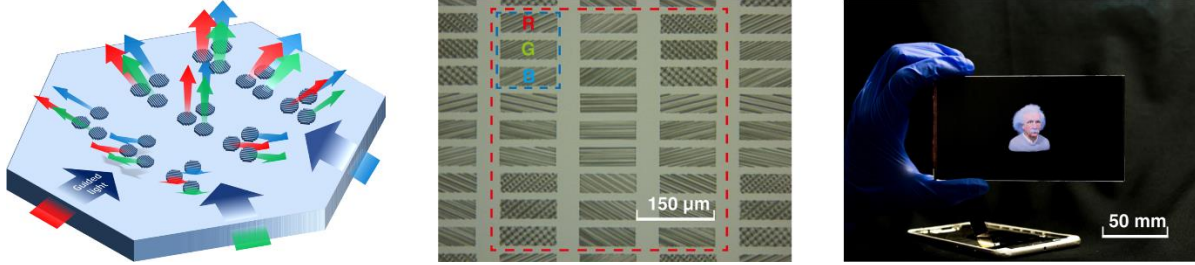
Box 3. Active metasurface enabled glasses-free 3-D display

Glasses-free 3-D display (or autostereoscopy) is a technology poised to reshape human-machine interactions. Unlike conventional display panels which reproduces only the intensity of light emanating from an object, an autostereoscopic display restores the light field information including both intensity and propagation direction. The schematic configuration of a 3-D light field display is depicted in the figure. A pixel modulates the light output intensity and at the same time directs emitted light in a specific direction. Therefore, the pixels can be grouped according to their emission directions such that each subset of pixels project a unique perspective view of the displayed scene along one viewing angle (and hence the name “multiview display”), thereby creating 3-D stereoscopic perception for users. Early prototypes of multiview display were implemented using parallax barriers, lenticular lenses or micro-lens arrays on top of flat display panels, although they face limitations in efficiency, FOV and depth of field. Moreover, spatial and angular resolutions represent an inherent trade-off, since the spatial resolution is reduced by a factor equaling to the number of angular views. The subpar spatial and angular resolution is a primary factor that degrades user experience.

The challenges encountered by traditional optics have fueled a growing interest in multiview displays based on flat optics. In 2013, a group from HP Laboratories reported a 3-D display technology using arrays of diffractive grating pixels in place of refractive optics³³, providing 64-view images within 90° FOV. Notwithstanding the passive nature of the grating pixels, they were integrated with an active LC shutter plane to perform dynamic image display. This pioneering innovation has been successfully commercialized by an HP spin-off Leia Inc.³⁴. Using metasurfaces as the light-directing pixels promises several additional benefits. While the efficiency of traditional diffraction gratings is limited by power dissipation into high-order diffraction, metasurfaces avoid undesirable diffraction orders to significantly boost efficiency and diminish background noise. The exceptional light bending capability of metasurfaces affords a large FOV without compromising efficiency. For example, recent work by Hua *et al.* demonstrated a metasurface-enabled full-color 3-D display prototype with a record 160° horizontal FOV³⁵. Metasurfaces also allow densely packed pixels with a large fill factor to improve display resolution without inducing excessive crosstalk, and they can further exploit temporal and polarization multiplexing schemes to alleviate the trade-off between spatial and angular resolution³⁶. Additionally, a metasurface pixel arrays with tunable light directing properties can be coupled with an eye tracking sensor such that the number of angular views broadcasted toward the observer is dynamically optimized. Yet another potential advantage offered by metasurfaces is the prospect of their monolithic integration on display pixels such as

micro-LEDs, which opens up unprecedented latitude for fine control of the emission light field^{37,38}.

In sum, scalable manufacturing and packaging of high-density, large-area metasurface pixel arrays remain the key enabling technology to resolve the resolution bottleneck of 3-D displays and catalyze their widespread adoption in next-generation consumer electronic devices.



(Left) Schematic design of a multi-view 3-D display panel consisting of metasurface pixel arrays³³; (middle) optical microscopy image of tri-color metasurface pixel arrays³⁵; (right) a full-color, video-rate 3-D display prototype³⁵.

Missing links: bridging the present and the prospect

Despite the explosive growth of active metasurface technologies over the past few years, several technological gaps still loom. Here we focus on three critical areas where more R&D efforts are mandated before the application prospects portrayed in the last section can be fulfilled.

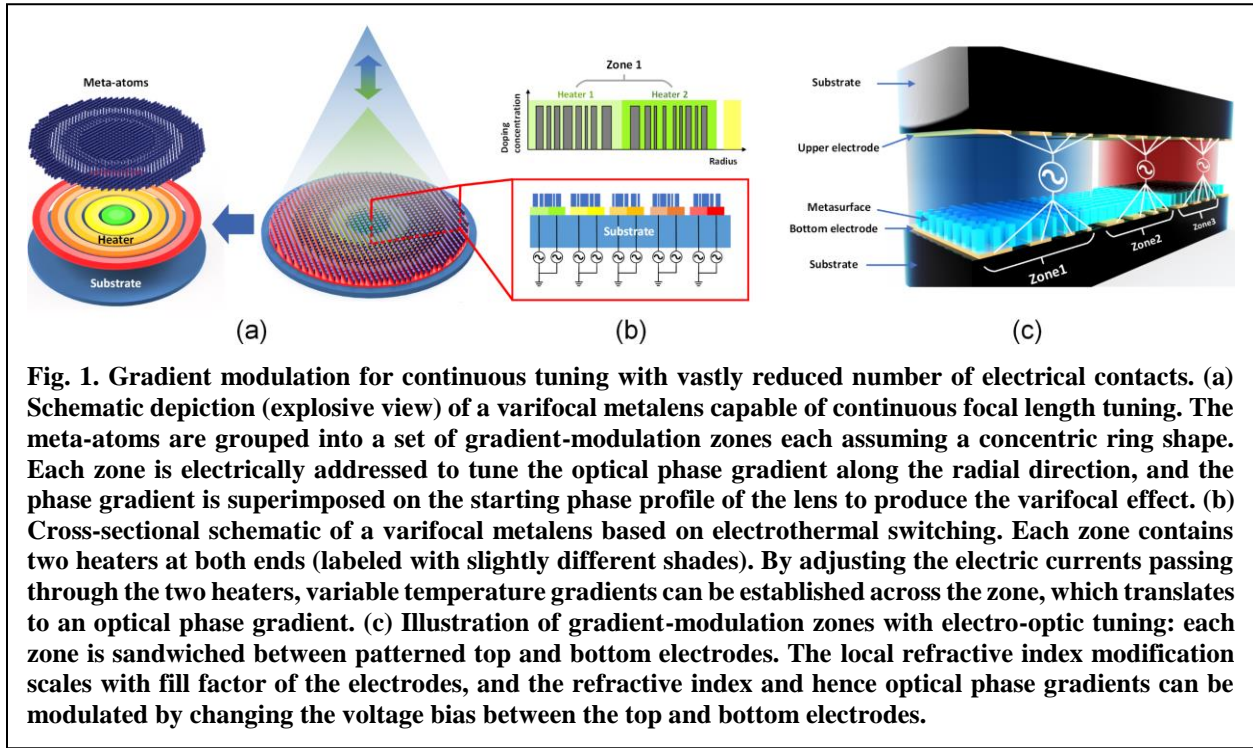
Scalable manufacturing and packaging

The first and foremost barrier lies in scalable manufacturing and packaging of active metasurfaces. Their passive counterparts used to encounter the same challenge: in the early phase of development, metasurfaces were almost exclusively prototyped in university cleanrooms using electron beam lithography with painstakingly low throughput. Recent advances have nonetheless circumvented this bottleneck, as fabrication of passive metasurfaces on full glass wafers have been validated via deep ultraviolet (DUV) lithography in standard silicon foundries^{50,51} and other high-throughput fabrication methods such as nanoimprint lithography are being explored as well. Manufacturing of active metasurfaces not only stipulates similar requirements on large-area, fine-line lithographic patterning, but is also appreciably more complicated than the passive counterpart. Therefore, commercially viable manufacturing practices of active metasurfaces must maximally leverage standard semiconductor foundry processing and packaging to manage the escalating fabrication and assembly complexity. The foundry manufacturing process may be complemented with backend integration to introduce new materials and functions, in which case the integration process shall capitalize on a mature industrial ecosystem (as summarized in Table 1) to access existing infrastructures, knowledge base, and supply chain to expedite the technology's learning curve.

Electrical addressing of large 2-D pixel arrays

Scaling the existing active metasurface technologies to electrically controlled, high-density and large-size 2-D pixel arrays marks another technical milestone. This is motivated by the demand for enhanced wavefront control with fine resolution: taking beam steering (Box 2) as an example, reducing pixel size contributes to expanding FOV and suppressing sidelobes. At the limit when each meta-atom can be individually tuned (i.e. one meta-atom per pixel), a 'universal' optic results, enabling not only continuous tuning but also reconfiguration of the metasurface to emulate arbitrary optics.

The Holy Grail of a ‘universal optic’, however, face major challenges in electrical wiring, cross-talk, and control complexity. A small (10×10 pixels) 2-D active metasurface array was demonstrated recently³², although the in-plane fan-out wiring design is not scalable to large arrays. A practical solution for large 2-D arrays involves integrating the pixels to a control backplane via vertical interconnect accesses to form a cross-bar matrix. In the case of volatile pixels, each pixel needs to be coupled with a transistor such that its can be individually tuned, analogous to the active matrix architecture in flat panel displays. For nonvolatile active metasurfaces, a simplified ‘passive matrix’ configuration without the transistor backplane is equally viable since the ‘set-and-forget’ pixels can be reconfigured sequentially row-by-row, albeit at the expense of refreshing rate. Notably, each pixel in a passive-matrix cross-bar array still requires a selector with nonlinear I-V characteristics to prevent sneak-path current, which can be implemented via semiconductor diodes or threshold switching phenomena in various materials.



It is worth mentioning that continuous tuning of a meta-optical element does not necessarily entail full 2-D matrix addressing. Here we propose a new concept of gradient modulation: instead of directly tuning the phase delay of meta-atom pixels, electrical contact pairs are used to generate an in-plane refractive index gradient in between each pair, which translates to a tunable phase gradient superimposed on the unmodulated metasurface phase profile. Figures 1b and 1c illustrate the electrode arrangement to produce the variable phase gradient in active metasurfaces based on electrothermal and electro-optic tuning mechanisms, respectively. A functional meta-optical device is assembled from a multitude of gradient-modulation zones defined by the electrode pairs. For instance, Fig. 1a depicts a varifocal metalens comprising zones of concentric ring shapes. The scalable design can dramatically reduce the number of electrical leads and hence wiring complexity compared to 2-D matrix addressing. As an example, we show that a metalens with 1 mm diameter partitioned into merely 23 gradient-modulation zones is capable of continuous focal length tuning from 2 mm to infinity at $2.2 \mu\text{m}$ wavelength while maintaining diffraction-limited

performance throughout (refer to Supplementary Information for more details). In contrast, 2-D addressing of a metalens of the same size involve a staggering half million active pixels!

Reliability is the key

Last but certainly not least comes reliability, a topic rarely deliberated in academic publications. Nevertheless, its importance to practical applications cannot be over-emphasized. The reliability requirement is illustrated in the example of automotive LiDAR (Box 2), whose durability qualifications under various environmental stresses are elaborately enumerated by international standards and manufacturers' specifications. For active metasurfaces, endurance is another critical parameter. As is evident from Tables 1 and 2, the endurances of many active metasurface technologies are still lagging application demands. Even for those labeled with 'very large' endurance, their reliability under realistic deployment conditions has often not been verified. On the bright side, unlike their passive counterparts whose performance is fixed post-fabrication, active metasurfaces allow reconfiguration or re-training of their design parameters to "adapt" to imperfections during the fabrication and operation processes, thereby significantly improving system robustness to maintain design goals.

Addressing the reliability challenge warrants scrupulous characterization of degradation kinetics in application-relevant environments, thorough material investigations to elucidate the pertinent failure mechanisms, and judicious device designs guided by the fundamental insights to improve robustness. The studies will inform the essential path for active metasurfaces to make a lasting impact on photonic applications.

New capabilities: beyond today's functional repertoire

In addition to filling the missing links, new research initiatives in the field are set to significantly expand the functionalities of active metasurface optics. In this section, we highlight two salient examples where such advances are anticipated to enhance their performances and open up novel application venues.

Dual modulation of phase and amplitude

Even though imparting a phase delay without incurring optical loss is a common design prescription for phase-gradient metasurfaces, there are scenarios where simultaneous phase and amplitude modulation comes in handy. In OPAs (Box 2), amplitude apodization helps to match the output field profile to that of a Gaussian beam to suppress sidelobes. In 3-D display (Box 3), the dual modulation is the prerequisite for complete light field manipulation. In analog optical computing, both phase and amplitude are often concurrently used to encode information¹.

A straightforward solution is to assign the amplitude and phase modulation functions to two cascaded active metasurfaces at the expense of fabrication complexity and optical efficiency. Alternatively, a dual-gate configuration has been applied to ITO metasurfaces to accommodate complex reflectance tuning by adjusting two gate voltages^{5,39}, although the coupled refractive index and absorption changes due to free carrier dispersion in ITO restricts the accessible tuning range. Resorting to two distinct mechanisms to separately engineer refractive index and loss furnishes far more versatile phase and amplitude control. Candidate materials include ionic conductors where migration of different ions produces tri-state switching with orthogonal optical property changes⁴⁰, and chalcogenide PCMs where crystallization and vacancy ordering account for decoupled refractive index and absorption modifications⁴¹.

Metasurface-augmented active photonics

While useful as standalone optical elements, the application scope of active metasurfaces can be significantly broadened once they can be seamlessly integrated with traditional optical or

optoelectronic components. Such metasurface-augmented photonics transcends intrinsic performance limits confronting metasurfaces, such as narrow spectral bandwidth and low quality factor (Q): combining metasurfaces with refractive or reflective optics overcomes their group delay limitation⁴² to support broadband operation⁴³, and embedding active meta-atoms inside a Fabry-Perot cavity maintains the otherwise wavelength-sensitive high-Q resonance condition across a wide tuning range. Besides the performance gains, metasurfaces further profit from their compatibility with monolithic or hybrid integration on optoelectronic platforms (e.g., lasers, detectors, planar photonic integrated circuits, as well as display and imaging arrays) compared to conventional refractive or diffractive elements. The integration can potentially leverage scalable semiconductor fabrication routes to access sophisticated electronic backplanes for massive array modulation. Moreover, some tuning operations (in particular amplitude modulation) can be offloaded to the optoelectronic components to simplify the meta-optical system while retaining active functionalities (e.g., in a metasurface-integrated micro-LED multi-view display alluded to in Box 3). We envision that the metasurface-augmented optoelectronic systems will confer novel capabilities such as pixel-level light field control and detection, computational imaging, high-resolution imaging spectroscopy, and neuromorphic computing.

Realizing the metasurface-augmented active photonics calls for innovative design and fabrication strategies. Specifically, two modeling frameworks are essential to metasurface-augmented photonics. One is a computationally efficient objective-driven method to approach this inherently multiscale – spanning six orders of magnitude in spatial dimensions – and multi-objective – as specified by the active tuning condition – design problem. A successful recipe will likely bridge classical ray based optimization of traditional optics and emerging full-wave inverse design techniques for sub-wavelength meta-structures^{44–46}. The other involves multi-physics *predictive* models linking the (electrical, thermal, mechanical, and/or optical) stimuli to the resulting active metasurface response, which becomes particularly important in treating complex material transformations where simple effective medium theory fails^{47,48}.

Advancing metasurface-augmented photonics also demands fabrication schemes commensurate with scalable manufacturing, such as conformal processing of active metasurfaces on both flat and curved surfaces of conventional optics, and monolithic integration routes of meta-optics on optoelectronic devices⁴⁹. We foresee that breakthroughs in scalable metasurface integration will catalyze new applications exploiting the best of two worlds in both conventional optics and metasurfaces.

Summary and outlook

Since their introduction in the past decade, active metasurfaces have swiftly taken the center stage in metamaterials research, boasting significantly enhanced and expanded functionalities over their passive counterparts. The extra layer of complexity needed for active tuning, however, presents an additional barrier to their deployment in the commercial domain.

To overcome the challenges, the imminent success of passive metasurfaces, whose practical applications start to surface, sets a paradigm. Over the past few years, the community have converged upon several potential beachhead markets of passive metasurfaces where their key competitive advantages – system-level SWaP benefits, minimal monochromatic aberration, polarization discrimination capacity, and low-cost at scale – are fully mobilized, and forged a path toward large-area, cost-effective manufacturing capitalizing on standard foundry processing. Likewise, leveraging existing semiconductor foundry infrastructures as well as mature ecosystems in adjacent industries provide a shortcut to facilitate scalable manufacturing and packaging of active metasurface devices. As active metasurfaces establish their manufacturing scalability and

reliability, industrial deployment of active metasurfaces will also be initiated first in niche applications, with several promising early examples discussed in the text, before percolating into established markets. In this process, new and unique functionalities exemplified by ‘universal optics’ consisting of 2-D active meta-atom pixel arrays, electronics and optoelectronics with monolithically integrated metasurface optics, and flat optics rendering complete active control of light phase and amplitude will continue to extend their application venues. The growing market demands will in turn drive the assimilation of active metasurface fabrication into mainstream foundry processes to further enhance yield, lower cost, and improve reliability toward widespread adoption of the technology. This is a bright prospect that the entire active metasurface community can and should strive for, as ‘the future depends on what we do in the present’.

Acknowledgments

This work was sponsored by the National Science Foundation under award number 2132929, Defense Advanced Research Projects Agency Defense Sciences Office Program: EXTREME Optics and Imaging (EXTREME) under agreement number HR00111720029, the National Institute of Aerospace, and Lockheed Martin Corporation Internal Research and Development. The authors would like to thank Sensong An and Fan Yang for assistance with optical modeling and Xiaochen Sun, Xu Fang, and Lei Bi for helpful technical discussions. The views, opinions and/or findings expressed are those of the authors and should not be interpreted as representing the official views or policies of the Department of Defense or the U.S. Government.

Author contributions

All authors contributed to writing the paper.

Competing financial interests

The authors declare no competing financial interests.

Table 1. Summary of active metasurface technologies (refer to Supplementary Information for more details and discussions)											
Type	Material or mechanism	Refractive index tuning range	Optical absorption	Endurance (cycling lifetime)	Failure mechanism limiting cycling lifetime	3-dB bandwidth or 10-90 rise/fall time	Speed limiting factor	Volatility	Foundry manufacturing compatibility	Potential challenges	Relevant industry ecosystem
Mechanical	Displacement	-	None	Very large	Mechanical failure	~ 1 Hz	Speed of mechanical motion	-	Compatible	Integration challenge	-
	Elastic deformation	-	None	15,000	Material fatigue or interface delamination	~ 1 Hz	Speed of mechanical motion	-	-	Reproducibility and stability	-
	MEMS actuation	-	None	> 10 ⁹	Material fatigue; stiction; delamination; wear	1 MHz	Resonant frequencies of mechanical eigenmodes	Design-dependent	Compatible	High voltage	MEMS
Free carrier density modulation (electrical injection)	Semiconductors (junction biasing)	0.08	Free carrier absorption (FCA)	Very large	-	0.18 MHz	Carrier transit time; RC delay	Volatile	Compatible with III-V foundry processes	Optical loss; small index change or optical modal overlap with the active region	Semiconductor
	TCOs (field gating)	1.39	FCA	Very large	-	10 MHz		Volatile	Backend processing available in selected foundries		Display
	2-D materials (field gating)	~ 1	Material absorption	Very large	-	> 1 GHz		Volatile (capacitive)	Backend integration currently under development		-
Thermo-optic	Semiconductors (thermal free-carrier refraction)	1.5	FCA	Likely large	-	5 kHz	Thermal time constant	Volatile	Compatible if only CMOS materials are used	Optical loss; relatively slow response	Integrated photonics
	Semiconductors or dielectric materials	0.15	Minor FCA due to carrier thermalization							Relatively slow response; large energy consumption	
Electro-optic	EO polymers	0.11	None	Very large	-	50 MHz	RC delay	Volatile (capacitive)	-	High voltage	-
	EO crystals	0.001	None	Very large	-	95 MHz	RC delay	Volatile (capacitive)	Backend processing available in selected foundries	Small modulation amplitude	Integrated photonics
	Liquid crystals	0.15	None	> 10 ¹⁰	-	350 Hz	Relaxation time of liquid crystal molecules	Volatile (capacitive)	Backend processing and packaging available	Relatively slow response	Display
	Semiconductor multi-quantum-well (quantum confined Stark effect)	~ 0.01	Electroabsorption dictated by the Kramers-Kronig relations	Very large	-	< 10 ns	RC delay	Volatile (capacitive)	Compatible with III-V foundry processes	Full 2 π phase coverage	III-V optoelectronics
Phase transition	VO ₂	Up to ~ 0.5 in visible and near-IR	FCA in the metallic state	> 24,000	Defect migration	450 fs / 2 ps	Kinetics of Mott transition or structural phase transition	Volatile	Backend processing available in selected foundries	Optical loss	-
	Chalcogenide PCMs	3.3 (Ge ₂ Sb ₂ Te ₅) 1.8 (Ge ₂ Sb ₂ Se ₄ Te)	None	> 5 \times 10 ⁵	Elemental segregation; cyclic strain	200 ns / 300 ns	Crystallization speed	Non-volatile	Backend processing available in selected foundries	High voltage	Memory
Electrochemical	Electrochromic polymers	0.7	Electronic absorption at the oxidized state	> 10 ⁷	Photochemical degradation	> 25 Hz	Ion transport kinetics in the polymer and electrolyte	Non-volatile	-	Relatively slow response; optical loss	Smart windows
	Ionic conducting oxides (protonation)	0.45 (SmNiO ₃) ~ 0.4 (GdO _x)	FCA in the metallic state	Several hundred	Dielectric breakdown; defect migration	13 ms	Ion transport kinetics; film thickness	Non-volatile	-	Endurance; relatively slow response	-
	Ionic conducting oxides (lithium intercalation)	~ 0.2 (WO ₃) 0.65 (TiO ₂)	FCA in the metallic state	400	Ion trapping	3 s	Ion transport kinetics; film thickness	Non-volatile	-	Endurance; slow response	Smart windows
	Metal electrodeposition	-	Absorption of electrodeposited metal	> 200	Metal oxidation	~ 1 Hz	Electrodeposition reaction rate	Non-volatile	-	Integration challenge	-
Chemical	Metals (hydrogenation)	~ 4 (Mg)	FCA	3,000	Strain due to volume change; oxidation and hydroxylation	~ 0.1 Hz	Hydrogen diffusion in metal; film thickness	Non-volatile	-	Integration challenge	-
	Cover material addition/removal	~ 0.5	None	> 10	Residue and contamination	Seconds to minutes	Speed of dissolution or removal process	Non-volatile	-	Integration challenge	-
Magnetic	Magnetooptical oxides	~ 0.01	None	Very large	-	5 GHz	Kinetics of magnetic domain wall motion	Both	-	Integration challenge	-
All-optical	Kerr nonlinearity	Light intensity dependent	Nonlinear absorption	Very large	-	40 fs	Ultrafast electronic nonlinearity	Volatile	Compatible if CMOS materials are used	Integration challenge	-
	Free carrier injection	0.14	FCA	Very large	-	~ 100 fs / 20 ps	Carrier lifetime	Volatile	Compatible if CMOS materials are used	Integration challenge	-

Table 2. Potential applications of active metasurfaces: green-yellow-gray colors indicate decreasing relevance of the metric to the target use case: very important-somewhat important-minimally relevant (refer to Supplementary Information for more details and discussions)

Application	Tuning scheme	Optical tuning parameter (phase/amplitude)	Optical contrast (relevant metrics)	Optical loss suppression	Endurance (cycling lifetime requirement)	Speed (bandwidth requirement)	Power consumption
Tunable filters for multispectral sensing	Continuous	Amplitude	Extinction ratio		10^7	1 kHz	
Beam steering for LiDAR	Continuous	Both	Full 2π phase tuning range		10^9	10 Hz	
Light field display	Continuous	Both	Field-of-view and image contrast		10^{10}	30 Hz	
Computational imaging	Discrete	Phase	Full 2π phase tuning range		10^{10}	100 Hz	
Optical neural network with adaptive network training	Continuous	Both	Full 2π phase tuning range		10^8	1 kHz	
Dynamic projection display	Continuous	Amplitude	Image contrast		10^{10}	30 Hz	
Electronic paper (reflective display)	Discrete or continuous	Amplitude	Color saturation and image contrast		10^7	1 Hz	Nonvolatile or capacitive
Zoom lens	Discrete or continuous	Phase	Full 2π phase tuning range		10^5	1 Hz	
Digital signal modulation for free-space communications	Discrete	Either	Modulation contrast		10^{18}	10 GHz	
Adaptive optics	Continuous	Phase	Full 2π phase tuning range		10^{10}	100 Hz	
Nonreciprocal optics based on spatiotemporal modulation	Discrete	Either	Isolation ratio		10^{18}	10 GHz	
Optical limiter	Discrete	Amplitude	Extinction ratio		Application-specific	> 1 GHz	Nonvolatile
Adaptive thermal camouflage	Continuous	Amplitude	Dynamic range		10^8	10 Hz	

References

1. Abdollahramezani, S., Hemmatyar, O. & Adibi, A. Meta-optics for spatial optical analog computing. *Nanophotonics* **9**, 4075–4095 (2020).
2. Salary, M. M. & Mosallaei, H. Time-Modulated Conducting Oxide Metasurfaces for Adaptive Multiple Access Optical Communication. *IEEE Trans. Antennas Propag.* **68**, 1628–1642 (2020).
3. Liu, Y. *et al.* Dynamic thermal camouflage via a liquid-crystal-based radiative metasurface. *Nanophotonics* **9**, 855–863 (2020).
4. Shalaginov, M. Y. *et al.* Reconfigurable all-dielectric metalens with diffraction-limited performance. *Nat. Commun.* **12**, 1225 (2021).
5. Park, J. *et al.* All-solid-state spatial light modulator with independent phase and amplitude control for three-dimensional LiDAR applications. *Nat. Nanotechnol.* **16**, 69–76 (2020).
6. Gyeongtae Kim *et al.* Metasurface-empowered spectral and spatial light modulation for disruptive holographic displays. *Nanoscale* **14**, 4380–4410 (2022).
7. Julian, M. N., Williams, C., Borg, S., Bartram, S. & Kim, H. J. Reversible optical tuning of GeSbTe phase-change metasurface spectral filters for mid-wave infrared imaging. *Optica* **7**, 746–754 (2020).
8. Wang, X., Díaz-Rubio, A., Li, H., Tretyakov, S. A. & Alù, A. Theory and Design of Multifunctional Space-Time Metasurfaces. *Phys. Rev. Appl.* **13**, 044040 (2020).
9. Huang, Y.-W. *et al.* Gate-Tunable Conducting Oxide Metasurfaces. *Nano Lett.* **16**, 5319–5325 (2016).
10. Weiss, A. *et al.* Tunable Metasurface Using Thin-Film Lithium Niobate in the Telecom Regime. *ACS Photonics* **9**, 605–612 (2022).
11. Wu, P. C. *et al.* Dynamic beam steering with all-dielectric electro-optic III–V multiple-quantum-well metasurfaces. *Nat. Commun.* **10**, 3654 (2019).
12. Bosch, M., Shcherbakov, M. R., Fan, Z. & Shvets, G. Polarization states synthesizer based on a thermo-optic dielectric metasurface. *J. Appl. Phys.* **126**, 073102 (2019).
13. Kaissner, R. *et al.* Electrochemically controlled metasurfaces with high-contrast switching at visible frequencies. *Sci. Adv.* **7**, eabd9450 (2021).
14. Xia, S. *et al.* Enhancement of the Faraday Effect and Magneto-optical Figure of Merit in All-Dielectric Metasurfaces. *ACS Photonics* (2022). doi:10.1021/ACSPHOTONICS.1C01692
15. Tripathi, A. *et al.* Tunable Mie-Resonant Dielectric Metasurfaces Based on VO₂ Phase-Transition Materials. *ACS Photonics* **8**, 1206–1213 (2021).
16. Zhang, Y. *et al.* Electrically reconfigurable non-volatile metasurface using low-loss optical phase-change material. *Nat. Nanotechnol.* **16**, 661–666 (2021).
17. Komar, A. *et al.* Dynamic Beam Switching by Liquid Crystal Tunable Dielectric Metasurfaces. *ACS Photonics* **5**, 1742–1748 (2018).
18. Colburn, S., Zhan, A. & Majumdar, A. Varifocal zoom imaging with large area focal length adjustable metalenses. *Optica* **5**, 825–831 (2018).
19. Malek, S. C., Ee, H.-S. & Agarwal, R. Strain Multiplexed Metasurface Holograms on a Stretchable Substrate. *Nano Lett.* **17**, 3641–3645 (2017).
20. Arbabi, E. *et al.* MEMS-tunable dielectric metasurface lens. *Nat. Commun.* **9**, 812 (2018).
21. Paniagua-Domínguez, R. *et al.* A Metalens with a Near-Unity Numerical Aperture. *Nano Lett.* **18**, 2124–2132 (2018).
22. Liang, H. *et al.* Ultrahigh Numerical Aperture Metalens at Visible Wavelengths. *Nano Lett.*

- 18**, 4460–4466 (2018).
23. Shalaginov, M. Y. *et al.* Single-Element Diffraction-Limited Fisheye Metalens. *Nano Lett.* **20**, 7429–7437 (2020).
24. Lin, Z. *et al.* End-to-end nanophotonic inverse design for imaging and polarimetry. *Nanophotonics* **10**, 1177–1187 (2021).
25. Arya, G. *et al.* End-to-End Optimization of Metasurfaces for Imaging with Compressed Sensing. *arXiv:2201.12348* (2022).
26. Shalaginov, M. Y. *et al.* Design for quality: reconfigurable flat optics based on active metasurfaces. *Nanophotonics* **9**, 3505–3534 (2020).
27. Williams, C., Hong, N., Julian, M., Borg, S. & Kim, H. J. Tunable mid-wave infrared Fabry-Perot bandpass filters using phase-change GeSbTe. *Opt. Express* **28**, 10583 (2020).
28. Rais-Zadeh, M. & Jafari, M. Zero-static-power phase-change optical modulator. *Opt. Lett.* **41**, 1177–1180 (2016).
29. Chung, H. & Miller, O. D. High-NA achromatic metalenses by inverse design. *Opt. Express* **28**, 6945–6965 (2020).
30. Li, S. Q. *et al.* Phase-only transmissive spatial light modulator based on tunable dielectric metasurface. *Science* **364**, 1087–1090 (2019).
31. Lumotive. Available at: <https://www.lumotive.com/>.
32. Kim, S. Il *et al.* Two-dimensional beam steering with tunable metasurface in infrared regime. *Nanophotonics* (2022). doi:10.1515/NANOPH-2021-0664/MACHINEREADABLECITATION/RIS
33. Fattal, D. *et al.* A multi-directional backlight for a wide-angle, glasses-free three-dimensional display. *Nature* **495**, 348–351 (2013).
34. Lume Pad 3D Lightfield Tablet | Leia Inc. Available at: <https://www.leiainc.com/>.
35. Hua, J. *et al.* Foveated glasses-free 3D display with ultrawide field of view via a large-scale 2D-metagrating complex. *Light Sci. Appl.* **10**, 213 (2021).
36. Hua, J., Qiao, W. & Chen, L. Recent Advances in Planar Optics-Based Glasses-Free 3D Displays. *Front. Nanotechnol.* **4**, 829011 (2022).
37. Khaidarov, E. *et al.* Control of LED Emission with Functional Dielectric Metasurfaces. *Laser Photon. Rev.* **14**, 1900235 (2020).
38. Joo, W. J. *et al.* Metasurface-driven OLED displays beyond 10,000 pixels per inch. *Science* **370**, 2022 (2020).
39. Kafaie Shirmanesh, G., Sokhoyan, R., Pala, R. A. & Atwater, H. A. Dual-Gated Active Metasurface at 1550 nm with Wide (>300°) Phase Tunability. *Nano Lett.* **18**, 2957–2963 (2018).
40. Lu, N. *et al.* Electric-field control of tri-state phase transformation with a selective dual-ion switch. *Nature* **546**, 124–128 (2017).
41. Zhang, Y. *et al.* Myths and truths about optical phase change materials: A perspective. *Appl. Phys. Lett.* **118**, 210501 (2021).
42. Presutti, F. & Monticone, F. Focusing on Bandwidth: Achromatic Metalens Limits. *Optica* **7**, 624–631 (2020).
43. Chen, W. T. *et al.* Broadband Achromatic Metasurface-Refractive Optics. *Nano Lett.* **18**, 7801–7808 (2018).
44. Wu, K., Coquet, P., Wang, Q. J. & Genevet, P. Modelling of free-form conformal metasurfaces. *Nat. Commun.* **9**, 3494 (2018).
45. Campbell, S. D. *et al.* Review of numerical optimization techniques for meta-device design

- [Invited]. *Opt. Mater. Express* **9**, (2019).
46. Li, Z. *et al.* Inverse design enables large-scale high-performance meta-optics reshaping virtual reality. *arXiv:2104.09702* (2021). doi:10.48550/arxiv.2104.09702
 47. Frame, J. D., Green, N. G. & Fang, X. Modified Maxwell Garnett model for hysteresis in phase change materials. *Opt. Mater. Express* **8**, 1988 (2018).
 48. Meyer, S., Tan, Z. Y. & Chigrin, D. N. Multiphysics simulations of adaptive metasurfaces at the meta-atom length scale. *Nanophotonics* **9**, 675–681 (2020).
 49. Kobayashi, F., Shikama, K., Miyata, M., Nemoto, N. & Hashimoto, T. Full-color-sorting metalenses for high-sensitivity image sensors. *Optica* **8**, 1596–1604 (2021).
 50. Park, J. S. *et al.* All-Glass, Large Metalens at Visible Wavelength Using Deep-Ultraviolet Projection Lithography. *Nano Lett.* **19**, 8673–8682 (2019).
 51. Hu, T. *et al.* CMOS-compatible a-Si metalenses on a 12-inch glass wafer for fingerprint imaging. *Nanophotonics* **9**, 823–830 (2020).

Active metasurfaces: lighting the path to commercial success

Tian Gu^{1,2,*}, Hyun Jung Kim^{3,4,*}, Clara Rivero-Baleine^{5,*}, and Juejun Hu^{1,2,*}

¹Department of Materials Science & Engineering, Massachusetts Institute of Technology, Cambridge, Massachusetts, USA

²Materials Research Laboratory, Massachusetts Institute of Technology, Cambridge, Massachusetts, USA

³National Institute of Aerospace, Hampton, Virginia, USA

⁴NASA Langley Research Center, Hampton, Virginia, USA

⁵Missiles and Fire Control, Lockheed Martin Corporation, Orlando, Florida, USA

*gutian@mit.edu, hyunjung.kim@nasa.gov, clara.rivero-baleine@lmco.com, hujuejun@mit.edu

Table S1. Extended summary of active metasurface technologies^a

Type	Material or mechanism	Refractive index tuning range	Optical absorption	Endurance (cycling lifetime)	Failure mechanism limiting cycling lifetime	3-dB bandwidth or 10-90 rise/fall time ^b	Speed limiting factor	Volatility	Foundry manufacturing compatibility	Potential challenges	Relevant industry ecosystem
Mechanical	Displacement	-	None ^c	Very large	Mechanical failure	~ 1 Hz	Speed of mechanical motion	-	Compatible	Integration challenge	-
	Elastic deformation	-	None ^c	15,000 [1]	Material fatigue or interface delamination	~ 1 Hz	Speed of mechanical motion	-	-	Reproducibility and stability	-
	MEMS actuation	-	None ^c	> 10 ⁹ [2]	Material fatigue; stiction; delamination; wear	1 MHz [2]	Resonant frequencies of mechanical eigenmodes	Design-dependent	Compatible	High voltage	MEMS
Free carrier density modulation (electrical injection)	Semiconductors (junction biasing)	0.08 [3] ^d	Free carrier absorption (FCA)	Very large [4] ^e	-	0.18 MHz [5]	Carrier transit time; RC delay	Volatile	Compatible with III-V foundry processes	Optical loss; small index change or optical modal overlap with the active region	Semiconductor
	TCOs (field gating) ^f	1.39 [6] ^g	FCA	Very large	-	10 MHz [7]		Volatile	Backend processing available in selected foundries		Display
	2-D materials (field gating)	~ 1 [8]	Material absorption	Very large	-	> 1 GHz [9]		Volatile (capacitive)	Backend integration currently under development [10]		-
Thermo-optic	Semiconductors (thermal free-carrier refraction)	1.5 [11] ^g	FCA	Likely large [12] ^h	-	5 kHz [13]	Thermal time constant	Volatile	Compatible if only CMOS materials are used	Optical loss; relatively slow response	Integrated photonics
	Semiconductors or dielectric materials	0.15 [14] ⁱ	Minor FCA due to carrier thermalization		-					Relatively slow response; large energy consumption	
Electro-optic	EO polymers	0.11 [15] ^j	None ^c	Very large	-	50 MHz [15,16]	RC delay	Volatile (capacitive)	-	High voltage	-
	EO crystals	0.001 [17]	None ^c	Very large	-	95 MHz [18]	RC delay	Volatile (capacitive)	Backend processing available in selected foundries [19,20]	Small modulation amplitude	Integrated photonics
	Liquid crystals	0.15 [21,22] ^k	None ^c	> 10 ¹⁰ ^l	-	350 Hz [23]	Relaxation time of liquid crystal molecules	Volatile (capacitive)	Backend processing and packaging available	Relatively slow response	Display
	Semiconductor multi-quantum-well (quantum confined Stark effect)	~ 0.01 [24]	Electroabsorption dictated by the Kramers-Kronig relations	Very large	-	< 10 ns [25]	RC delay	Volatile (capacitive)	Compatible with III-V foundry processes	Full 2 π phase coverage	III-V optoelectronics
Phase transition	VO ₂	Up to ~ 0.5 in visible and near-IR [26,27]	FCA in the metallic state	> 24,000 [28] ^m	Defect migration [29]	450 fs / 2 ps [30] [†]	Kinetics of Mott transition or structural phase transition ⁿ	Volatile ^o	Backend processing available in selected foundries	Optical loss	-
	Chalcogenide PCMs	3.3 (Ge ₂ Sb ₂ Te ₃) [31] ^p 1.8 (Ge ₂ Sb ₂ Se ₄ Te) [32] ^p	None [32] ^c	> 5 \times 10 ⁵ [33] ^q	Elemental segregation; cyclic strain [34]	200 ns / 300 ns [35] [†]	Crystallization speed [36]	Non-volatile ^r	Backend processing available in selected foundries [37,38]	High voltage	Memory
Electrochemical	Electrochromic polymers	0.7 [39] ^s	Electronic absorption at the oxidized state	> 10 ⁷ [40]	Photochemical degradation [41]	> 25 Hz [40] ^t	Ion transport kinetics in the polymer and electrolyte [42]	Non-volatile	-	Relatively slow response; optical loss	Smart windows
	Ionic conducting oxides (protonation)	0.45 (SmNiO ₃) [43] ^p ~ 0.4 (GdO _x) [44] ^u	FCA in the metallic state	Several hundred [44] ^v	Dielectric breakdown [44]; defect migration	13 ms [44]	Ion transport kinetics; film thickness	Non-volatile	-	Endurance; relatively slow response	-
	Ionic conducting oxides (lithium intercalation)	~ 0.2 (WO ₃) [45] ^u 0.65 (TiO ₂) [46] ^w	FCA in the metallic state	400 [46]	Ion trapping [47]	3 s [48]	Ion transport kinetics; film thickness	Non-volatile	-	Endurance; slow response	Smart windows
	Metal electrodeposition	-	Absorption of electrodeposited metal	> 200 [49] ^x	Metal oxidation	~ 1 Hz [49]	Electrodeposition reaction rate	Non-volatile	-	Integration challenge	-
Chemical	Metals (hydrogenation)	~ 4 (Mg) [50] ^p	FCA	3,000 [51]	Strain due to volume change; oxidation and hydroxylation	~ 0.1 Hz [52]	Hydrogen diffusion in metal; film thickness [53]	Non-volatile	-	Integration challenge	-
	Cover material addition/removal	~ 0.5 [54,55]	None ^c	> 10 [56]	Residue and contamination [57]	Seconds to minutes	Speed of dissolution or removal process	Non-volatile	-	Integration challenge	-
Magnetic	Magnetooptical oxides	~ 0.01 [58]	None ^c	Very large	-	5 GHz [59] ^y	Kinetics of magnetic domain wall motion	Both	-	Integration challenge	-
All-optical	Kerr nonlinearity	Light intensity dependent	Nonlinear absorption	Very large	-	40 fs [60]	Ultrafast electronic nonlinearity	Volatile	Compatible if CMOS materials are used	Integration challenge	-
	Free carrier injection	0.14 [61]	FCA	Very large	-	~ 100 fs / 20 ps [62] [†]	Carrier lifetime	Volatile	Compatible if CMOS materials are used	Integration challenge	-

^a Here we focus on active metasurfaces operating in the optical frequency range, specifically from ultraviolet to long-wave infrared (excluding the terahertz spectrum). Only experimental demonstrations are included in the table.

^b In the case of active metasurfaces with asymmetric rise/fall responses (marked with [†]), both rise and fall time values are reported.

^c Here ‘none’ implies that the optical loss *can* be negligible throughout the entire active tuning cycle. However, this condition does not necessarily hold for all materials or devices belonging to the category.

^d Refractive index change of Si at 1550 nm wavelength with 10²⁰/cm³ hole concentration

^e Wear-out failure rates of semiconductor modulator devices have been found to be negligible (below 1 Failures in Time, FIT).

^f In addition to TCO, the same field gating configuration can also be applied to modulate carrier concentrations in semiconductor materials to realize optical tuning within their optical transparency window, for example in [124].

^g The refractive index change was amplified by operating near the epsilon-near-zero (ENZ) point.

^h Thermo-optic devices exhibit minimal degradation after 5,000 hours of accelerated aging tests.

ⁱ Index change in a Si metasurface when temperature increases from 300 K to 800 K at 1.1 μ m wavelength.

^j Index change quoted at 1500 nm wavelength for an applied electric field varying from -100 to 100 V/ μ m

^k Refractive index change of E7 liquid crystal (from Merck, a formulation commonly used in active metasurfaces) in the near-infrared when transitioning from the nematic to the isotropic phase.

^l While the lifetime of liquid crystal metasurfaces has not been extensively investigated, commercial liquid crystal displays usually specify a lifetime of up to 60,000 hours, which at 60 Hz refresh rate corresponds to > 10¹⁰ switching cycles.

^m Over 6.8 \times 10⁸ switching cycles have been demonstrated in VO₂-based RF switches [125].

ⁿ Mott-Hubbard type phase transition induced by optical pumping of carriers exhibits ultrafast transition kinetics down to 26 fs [126]. In contrast, structural phase transition in VO₂ is slower and occurs at a sub-nanosecond time scale or longer [127].

^o VO₂ devices can operate in a nonvolatile mode within a finite temperature range defined by its phase-transition hysteresis [128].

^p Refractive index change at 1550 nm wavelength.

^q Endurance values of over 1.5 \times 10⁸ and > 2 \times 10¹² have been demonstrated in RF switches [35] and electronic phase change memories [129] based on chalcogenide materials, respectively.

^r Volatility of switching phase change materials can be tuned by adjusting pulse parameters [130].

^s Refractive index change at 633 nm wavelength.

^t Switching time down to 100 μ s has been observed in polyaniline (PANI) [131].

^u Refractive index change at 400-800 nm wavelengths.

^v In memristive electronic device made of the rare earth nickelate NdNiO₃, stable performance over 1.6 \times 10⁶ cycles have been demonstrated [132].

^w Refractive index change at 649 nm wavelength associated with transition from TiO₂ to Li_{0.5}TiO₂.

^x 5,500 reversible electrodeposition cycles of metals have been realized in large-area smart windows [133].

^y Here the magnetic state is controlled by ultrafast optical excitation. Current driven magnetic switching with a 3-dB bandwidth of 6 GHz has been achieved in integrated magnetooptical waveguide modulators at cryogenic temperatures [134].

Table 2. Potential applications of active metasurfaces [63–77]: green-yellow-gray colors indicate decreasing relevance of the metric to the target use case: very important-somewhat important-minimally relevant (refer to Supplementary Information for more details and discussions)

Application	Tuning scheme	Optical tuning parameter (phase/amplitude) ^a	Optical contrast (relevant metrics)	Optical loss suppression	Endurance (cycling lifetime requirement)	Speed (bandwidth requirement)	Power consumption
Tunable filters for multispectral sensing [78–80]	Continuous	Amplitude	Extinction ratio		10^7 ^b	1 kHz ^c	
Beam steering for LiDAR [81,82]	Continuous	Both	Full 2π phase tuning range ^d		10^9 ^e	10 Hz	
Light field display [83–85]	Continuous	Both	Field-of-view and image contrast		10^{10} ^f	30 Hz ^g	
Computational imaging [86]	Discrete	Phase	Full 2π phase tuning range		10^{10} ^{ee}	100 Hz ^h	
Optical neural network with adaptive network training [87,88]	Continuous	Both	Full 2π phase tuning range		10^8 ⁱ	1 kHz	
Dynamic projection display [89–91]	Continuous	Amplitude	Image contrast		10^{10} ^{ee}	30 Hz ^{ff}	
Electronic paper (reflective display) [92–94]	Discrete or continuous	Amplitude	Color saturation and image contrast		10^7 ^j	1 Hz	Nonvolatile or capacitive
Zoom lens [95]	Discrete or continuous	Phase	Full 2π phase tuning range		10^5 ^k	1 Hz	
Digital signal modulation for free-space communications [15,96,97]	Discrete	Either	Modulation contrast		10^{18} ^l	10 GHz	
Adaptive optics [98]	Continuous	Phase	Full 2π phase tuning range		10^{10} ^m	100 Hz [99]	
Nonreciprocal optics based on spatiotemporal modulation [100–102]	Discrete	Either	Isolation ratio		10^{18} ^{kk}	10 GHz	
Optical limiter [103,104]	Discrete	Amplitude	Extinction ratio		Application-specific	> 1 GHz	Nonvolatile
Adaptive thermal camouflage [105,106]	Continuous	Amplitude	Dynamic range		10^8 ⁿ	10 Hz ^o	

^a Note that amplitude modulation can be implemented with phase modulation via interference effects although the reverse is not true: phase modulation cannot be realized by amplitude modulation alone.

^b Taking the Stratospheric Aerosol and Gas Experiment as an example, the science observation events are a maximum length of 6 minutes, and the filter will be switched 5 times per second during the event. Normal low earth orbits are approximately 90 minutes long, and one science observation event will take place per orbit. Approximately 10^7 cycles are performed per year on orbit based on the estimation.

^c Specification of high-speed motorized filter wheels (~ 1 ms per filter).

^d It is possible to realized beam steering (or generally other optical functions as well) with phase coverage well below 2π albeit at the expense of optical performance [135–137].

^e Assume 20-year lifetime with 5 hour daily use at 10 Hz frame rate.

^f Assume 100,000-hour lifetime (comparable to that of state-of-the-art display modules) at 30 Hz frame rate.

^g National Television Standards Committee (NTSC) video frame rate.

^h The speed must be higher than the frame rate of single images.

ⁱ Assume 10,000 in-situ adaptive training iterations, 10 meta-optics layers, and 100 reconfigurations.

^j Comparable to the lifetime of E-ink displays.

^k Typical mechanical lenses are capable of $\sim 100,000$ cycles.

^l Assume 5-year lifetime at 10 GHz modulation.

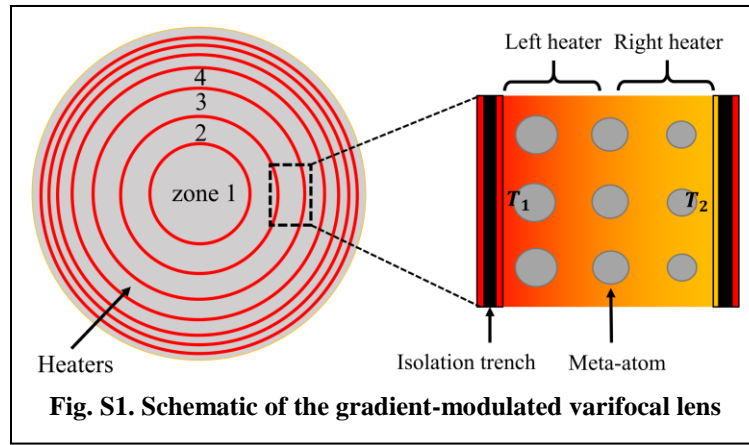
^m Assume 30,000 hour lifetime at 100 Hz.

ⁿ Assume 3,000 hour lifetime at 10 Hz.

^o The speed needs to be at least better than that of low frame rate infrared cameras which is generally specified at 9 Hz.

Continuous tuning via gradient modulation: managing electrical addressing complexity

The basic concept of gradient modulation is discussed in the main text. One important aspect of the design is that the optical phase profile of the metasurface device is numerically optimized at each optical state rather than analytically defined *a priori*. In the metalens example, it means that the phase profiles do not assume the classical hyperbolic form; instead, a direct search algorithm was employed to optimize the phase gradient in each zone to maximize the optical intensity at the focal spot without constraining the phase [107–111]. The division of the zones is also not defined analytically *a priori* but instead optimized to maximize the mean Strehl ratio of the focal spots. We note that this approach is also conceptually reminiscent of the ‘zone engineering’ scheme for achromatic metalens design in that the optimized phase profiles are piece-wise smooth with abrupt changes at the zone boundaries [112].



backplane [38,113–115]. Alternatively, other transparent heater materials such as transparent conducting oxides [116–118] and graphene [119,120] can also be used. The doping region is lithographically patterned, which can be implemented using a patterned SiO₂ layer as a mask during ion implantation. To generate a temperature gradient across a gradient-modulation zone along the radial direction, we patterned two doped heaters, one at each end of a zone. The widths of the doped regions (with the shape of a set of concentric rings) are chosen such that when the two heaters are separately biased, a nearly uniform temperature gradient is established throughout the entire zone. As an example, Fig. S2a plots the doping profile along the radial direction in a zone, where the doped regions belonging to the two heaters are labeled with different colors. The doped regions are connected in parallel within each heater. By applying different voltages at the two heaters, steady-state temperature profiles between 280 °C and 360 °C with varying gradients can be attained (Fig. S2b). Since we have previously quantified how the refractive index change in a PCM due to structural transition depends on the annealing temperature [36], the thermal gradient translates to locally varying refractive indices of the PCM, in this specific case Ge₂Sb₂Se₄Te or GSST [32,121,122]. The index change then modifies the

As an example illustrating the gradient modulation design, we consider a PCM-based transmissive active metalens (Fig. S1). The PCM meta-atoms are patterned on a silicon-on-insulator (SOI) substrate, and the SOI layer is selectively doped to create electrically conductive channels in order to electrothermally trigger structural transitions in the PCM meta-atoms. Here the SOI layer acts as an infrared-transparent resistive heater

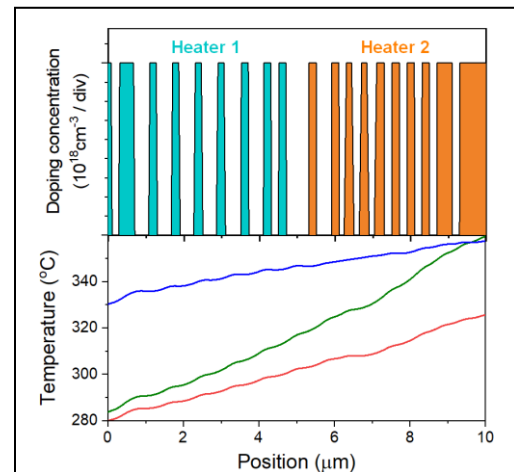


Fig. S2. (Top) doping and (bottom) temperature profiles across the zone when three different pairs of voltages are applied at the two heaters.

optical phase delay imparted by PCM meta-atoms, enabling full 2π phase tuning range as the meta-atoms are progressively transformed from amorphous to crystalline state [123]. This mechanism thus allows a variable ‘titled’ phase profile to be superimposed onto the starting phase distribution in each zone. By optimizing the variable phase gradient in each zone, we show that the focal length of the lens can be tuned to arbitrary values in a pre-defined range (2 mm to infinity in this design example). Figures S3a shows the simulated Strehl ratio of the varifocal metalens as a function of focal length f , and Figs. S3b and S3c plot the intensity profiles of the focal spot at $f = 2$ mm and $f = 6$ mm. The results indicate that the lens maintains diffraction-limited performance with a Strehl ratio greater than 0.9 throughout the tuning range, confirming the excellent optical quality of the varifocal metalens following the gradient modulation design.

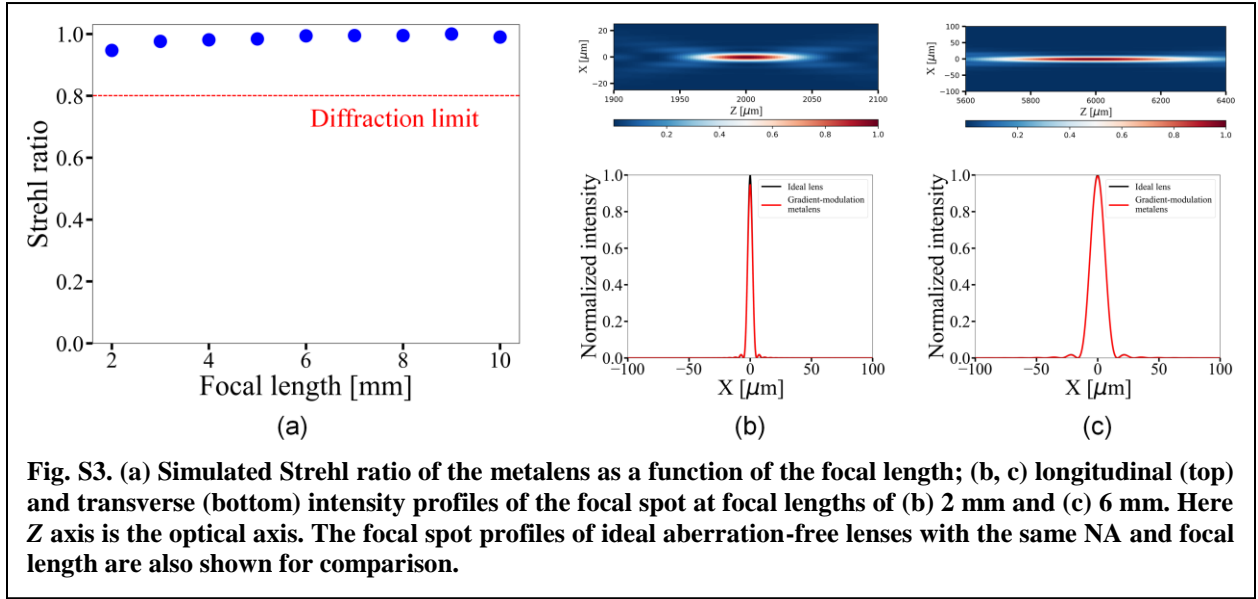


Fig. S3. (a) Simulated Strehl ratio of the metalens as a function of the focal length; (b, c) longitudinal (top) and transverse (bottom) intensity profiles of the focal spot at focal lengths of (b) 2 mm and (c) 6 mm. Here Z axis is the optical axis. The focal spot profiles of ideal aberration-free lenses with the same NA and focal length are also shown for comparison.

References

1. L. Martin-Monier, T. Das Gupta, W. Yan, S. Lacour, and F. Sorin, "Nanoscale Controlled Oxidation of Liquid Metals for Stretchable Electronics and Photonics," *Adv. Funct. Mater.* **31**, 2006711 (2021).
2. A. L. Holsteen, A. F. Cihan, and M. L. Brongersma, "Temporal color mixing and dynamic beam shaping with silicon metasurfaces," *Science* **365**, 257–260 (2019).
3. R. Soref and B. Bennett, "Electrooptical effects in silicon," *IEEE J. Quantum Electron.* **23**, 123–129 (1987).
4. A. Mekis, G. Armijo, J. Balardeta, B. Chase, Y. Chi, A. Dahl, P. De Dobbelaere, Y. De Koninck, S. Denton, M. Eker, S. Fathpour, D. Foltz, S. Gloeckner, K. Y. Hon, S. Hovey, S. Jackson, W. Li, Y. Liang, M. Mack, G. Masini, G. McGee, S. Pang, M. Peterson, T. Pinguet, L. Planchon, K. Roberson, N. Rudnick, S. Sahni, J. Schramm, C. Sohn, K. Stechschulte, P. Sun, G. Vastola, S. Wang, G. Wong, K. Yokoyama, S. Yu, and R. Zhou, "Silicon integrated photonics reliability," in *Optics InfoBase Conference Papers* (Optica Publishing Group, 2017), Vol. Part F52-I, p. IW3A.3.
5. P. P. Iyer, M. Pendharkar, C. J. Palmstrøm, and J. A. Schuller, "III–V Heterojunction Platform for Electrically Reconfigurable Dielectric Metasurfaces," *ACS Photonics* **6**, 1345–1350 (2019).
6. E. Feigenbaum, K. Diest, and H. A. Atwater, "Unity-Order Index Change in Transparent Conducting Oxides at Visible Frequencies," *Nano Lett.* **10**, 2111–2116 (2010).
7. Y.-W. Huang, H. W. H. Lee, R. Sokhoyan, R. A. Pala, K. Thyagarajan, S. Han, D. P. Tsai, and H. A. Atwater, "Gate-Tunable Conducting Oxide Metasurfaces," *Nano Lett.* **16**, 5319–5325 (2016).
8. N. K. Emani, T.-F. Chung, X. Ni, A. V. Kildishev, Y. P. Chen, and A. Boltasseva, "Electrically Tunable Damping of Plasmonic Resonances with Graphene," *Nano Lett.* **12**, 5202–5206 (2012).
9. B. Zeng, Z. Huang, A. Singh, Y. Yao, A. K. Azad, A. D. Mohite, A. J. Taylor, D. R. Smith, and H. T. Chen, "Hybrid graphene metasurfaces for high-speed mid-infrared light modulation and single-pixel imaging," *Light Sci. Appl.* **7**, 51 (2018).
10. D. Akinwande, C. Huyghebaert, C. H. Wang, M. I. Serna, S. Goossens, L. J. Li, H. S. P. Wong, and F. H. L. Koppens, "Graphene and two-dimensional materials for silicon technology," *Nature* **573**, 507–518 (2019).
11. P. P. Iyer, M. Pendharkar, C. J. Palmstrøm, and J. A. Schuller, "Ultrawide thermal free-carrier tuning of dielectric antennas coupled to epsilon-near-zero substrates," *Nat. Commun.* **8**, 472 (2017).
12. T. Goh, "Recent advances in large-scale silica-based thermo-optic switches," in *SPIE Proceedings* (SPIE, 2001), Vol. 4582, pp. 49–56.
13. Y. Horie, A. Arbabi, E. Arbabi, S. M. Kamali, and A. Faraon, "High-Speed, Phase-Dominant Spatial Light Modulation with Silicon-Based Active Resonant Antennas," *ACS Photonics* **5**, 1711–1717 (2018).
14. T. Lewi, N. A. Butakov, and J. A. Schuller, "Thermal tuning capabilities of semiconductor metasurface resonators," *Nanophotonics* **8**, 331–338 (2018).
15. I. C. Benea-Chelmus, M. L. Meretska, D. L. Elder, M. Tamagnone, L. R. Dalton, and F. Capasso, "Electro-optic spatial light modulator from an engineered organic layer," *Nat. Commun.* **12**, 5928 (2021).
16. T. Tanemura, J. Zhang, Y. Kosugi, M. Ogasawara, and Y. Nakano, "Metasurface high-speed

- modulators using electro-optic polymer," in *SPIE Proceedings* (SPIE, 2021), Vol. 11692, p. 1169208.
17. A. Karvounis, V. V. Vogler-Neuling, F. U. Richter, E. Dénervaud, M. Timofeeva, R. Grange, A. Karvounis, V. V. Vogler-Neuling, F. U. Richter, E. Dénervaud, M. Timofeeva, and R. Grange, "Electro-Optic Metasurfaces Based on Barium Titanate Nanoparticle Films," *Adv. Opt. Mater.* **8**, 2000623 (2020).
 18. A. Karvounis, V. V. Vogler-Neuling, and R. Grange, "95 MHz Bandwidth Electro-Optic Metasurfaces based on Barium Titanate Nanocrystals," in *2021 Conference on Lasers and Electro-Optics, CLEO 2021 - Proceedings* (Optica Publishing Group, 2021), p. FTh4K.5.
 19. A. Pomerene, A. Starbuck, A. Lentine, C. Dallo, C. T. DeRose, D. Hood, D. C. Trotter, H. Cai, M. Gehl, N. Boynton, S. Arterburn, and T. Friedmann, "A heterogeneously integrated silicon photonic/lithium niobate travelling wave electro-optic modulator," *Opt. Express* **28**, 1868–1884 (2020).
 20. M. Churaev, A. Riedhauser, R. N. Wang, C. Möhl, T. Blésin, M. A. Anderson, V. Snigirev, A. Siddharth, Y. Popoff, U. Drechsler, D. Caimi, S. Hönl, J. Riemensberger, J. Liu, P. Seidler, and T. J. Kippenberg, "Heterogeneously integrated lithium niobate photonics," *arXiv:2112.02018* (2021).
 21. J. Li, S. T. Wu, S. Brugioni, R. Meucci, and S. Faetti, "Infrared refractive indices of liquid crystals," *J. Appl. Phys.* **97**, 073501 (2005).
 22. O. Buchnev, N. Podoliak, M. Kaczmarek, N. I. Zheludev, and V. A. Fedotov, "Electrically Controlled Nanostructured Metasurface Loaded with Liquid Crystal: Toward Multifunctional Photonic Switch," *Adv. Opt. Mater.* **3**, 674–679 (2015).
 23. R. Kowerdziej, J. Wróbel, and P. Kula, "Ultrafast electrical switching of nanostructured metadvice with dual-frequency liquid crystal," *Sci. Rep.* **9**, 20367 (2019).
 24. P. C. Wu, R. A. Pala, G. Kafaie Shirmanesh, W. H. Cheng, R. Sokhoyan, M. Grajower, M. Z. Alam, D. Lee, and H. A. Atwater, "Dynamic beam steering with all-dielectric electro-optic III–V multiple-quantum-well metasurfaces," *Nat. Commun.* **10**, 3654 (2019).
 25. J. Lee, S. Jung, P. P.-Y. Chen, F. Lu, F. Demmerle, G. Boehm, M. M.-C. Amann, A. Alù, M. A. Belkin, J. Lee, S. Jung, P. P.-Y. Chen, F. Lu, A. Alù, M. A. Belkin, F. Demmerle, G. Boehm, and M. M.-C. Amann, "Ultrafast Electrically Tunable Polaritonic Metasurfaces," *Adv. Opt. Mater.* **2**, 1057–1063 (2014).
 26. M. Currie, M. A. Mastro, and V. D. Wheeler, "Characterizing the tunable refractive index of vanadium dioxide," *Opt. Mater. Express* **7**, 1697 (2017).
 27. C. Wan, Z. Zhang, D. Woolf, C. M. Hessel, J. Rensberg, J. M. Hensley, Y. Xiao, A. Shahsafi, J. Salman, S. Richter, Y. Sun, M. M. Qazilbash, R. Schmidt-Grund, C. Ronning, S. Ramanathan, and M. A. Kats, "On the Optical Properties of Thin-Film Vanadium Dioxide from the Visible to the Far Infrared," *Ann. Phys.* **531**, 1900188 (2019).
 28. Z. Zhu, P. G. Evans, R. F. Haglund, and J. G. Valentine, "Dynamically Reconfigurable Metadvice Employing Nanostructured Phase-Change Materials," *Nano Lett.* **17**, 4881–4885 (2017).
 29. A. G. Shabalin, J. del Valle, N. Hua, M. J. Cherukara, M. V Holt, I. K. Schuller, O. G. Shpyrko, A. G. Shabalin, J. del Valle, N. Hua, I. K. Schuller, O. G. Shpyrko, M. J. Cherukara, and M. V Holt, "Nanoscale Imaging and Control of Volatile and Non-Volatile Resistive Switching in VO₂," *Small* **16**, 2005439 (2020).
 30. T. Kang, Z. Ma, J. Qin, Z. Peng, W. Yang, T. Huang, S. Xian, S. Xia, W. Yan, Y. Yang, Z. Sheng, J. Shen, C. Li, L. Deng, and L. Bi, "Large-scale, power-efficient Au/VO₂ active

- metasurfaces for ultrafast optical modulation," *Nanophotonics* **10**, 909–918 (2020).
31. H. J. Kim, J. Sohn, N. Hong, C. Williams, and W. Humphreys, "PCM-net: a refractive index database of chalcogenide phase change materials for tunable nanophotonic device modelling," *J. Phys. Photonics* **3**, 024008 (2021).
32. Y. Zhang, J. B. Chou, J. Li, H. Li, Q. Du, A. Yadav, S. Zhou, M. Y. Shalaginov, Z. Fang, H. Zhong, C. Roberts, P. Robinson, B. Bohlin, C. Ríos, H. Lin, M. Kang, T. Gu, J. Warner, V. Liberman, K. Richardson, and J. Hu, "Broadband transparent optical phase change materials for high-performance nonvolatile photonics," *Nat. Commun.* **10**, 4279 (2019).
33. J. Meng, N. Peserico, X. Ma, Y. Zhang, C.-C. Popescu, M. Kang, M. Miscuglio, K. Richardson, J. Hu, and V. J. Sorger, "Electrical Programmable Low-loss high cyclable Nonvolatile Photonic Random-Access Memory," *arXiv:2203.13337* (2022).
34. L. Martin-Monier, C.-C. Popescu, L. Ranno, B. Mills, S. Geiger, D. Callahan, M. Moebius, and J. Hu, "Endurance of Chalcogenide Optical Phase Change Materials: a Review," *Opt. Mater. Express* **12**, 2145–2167 (2022).
35. J.-S. Moon, H.-C. Seo, K. K. Son, E. Yalon, K. Lee, E. Flores, G. Candia, and E. Pop, "Reconfigurable infrared spectral imaging with phase change materials," *SPIE Proc.* **10982**, 32 (2019).
36. Y. Zhang, C. Ríos, M. Y. Shalaginov, M. Li, A. Majumdar, T. Gu, and J. Hu, "Myths and truths about optical phase change materials: A perspective," *Appl. Phys. Lett.* **118**, 210501 (2021).
37. J. Choe, "Intel's 2nd Generation XPoint Memory | TechInsights," <https://www.techinsights.com/blog/memory/intels-2nd-generation-xpoint-memory>.
38. C. Ríos, Q. Du, Y. Zhang, C.-C. Popescu, M. Y. Shalaginov, P. Miller, C. Roberts, M. Kang, K. A. Richardson, T. Gu, S. A. Vitale, and J. Hu, "Ultra-compact nonvolatile photonics based on electrically reprogrammable transparent phase change materials," *arXiv:2105.06010* (2021).
39. R. Greef, M. Kalaji, and L. M. Peter, "Ellipsometric studies of polyaniline growth and redox cycling," *Faraday Discuss. Chem. Soc.* **88**, 277–289 (1989).
40. K. Xiong, O. Olsson, J. Svirielis, C. Palasingh, J. Baumberg, A. Dahlin, K. Xiong, J. Baumberg, O. Olsson, J. Svirielis, C. Palasingh, and A. Dahlin, "Video Speed Switching of Plasmonic Structural Colors with High Contrast and Superior Lifetime," *Adv. Mater.* **33**, 2103217 (2021).
41. J. Jensen, M. V. Madsen, and F. C. Krebs, "Photochemical stability of electrochromic polymers and devices," *J. Mater. Chem. C* **1**, 4826–4835 (2013).
42. J. Heinze, B. A. Frontana-Urbe, and S. Ludwigs, "Electrochemistry of Conducting Polymers—Persistent Models and New Concepts†," *Chem. Rev.* **110**, 4724–4771 (2010).
43. Z. Li, Y. Zhou, H. Qi, Q. Pan, Z. Zhang, N. N. Shi, M. Lu, A. Stein, C. Y. Li, S. Ramanathan, and N. Yu, "Correlated Perovskites as a New Platform for Super-Broadband-Tunable Photonics," *Adv. Mater.* **28**, 9117–9125 (2016).
44. M. Huang, A. Jun Tan, F. Büttner, H. Liu, Q. Ruan, W. Hu, C. Mazzoli, S. Wilkins, C. Duan, J. K. W. Yang, and G. S. D. Beach, "Voltage-gated optics and plasmonics enabled by solid-state proton pumping," *Nat. Commun.* **10**, 5030 (2019).
45. Y. Li, J. Van De Groep, A. A. Talin, and M. L. Brongersma, "Dynamic Tuning of Gap Plasmon Resonances Using a Solid-State Electrochromic Device," *Nano Lett.* **19**, 7988–7995 (2019).
46. J. Eaves-Rathert, E. Kovalik, C. F. Ugwu, B. R. Rogers, C. L. Pint, and J. G. Valentine,

- "Dynamic Color Tuning with Electrochemically Actuated TiO₂ Metasurfaces," *Nano Lett.* **22**, 1626–1632 (2022).
47. R. T. Wen, C. G. Granqvist, and G. A. Niklasson, "Eliminating degradation and uncovering ion-trapping dynamics in electrochromic WO₃ thin films," *Nat. Mater.* **14**, 996–1001 (2015).
 48. E. Hopmann and A. Y. Elezzabi, "Plasmochromic Nanocavity Dynamic Light Color Switching," *Nano Lett.* **20**, 1876–1882 (2020).
 49. G. Wang, X. Chen, S. Liu, C. Wong, and S. Chu, "Mechanical Chameleon through Dynamic Real-Time Plasmonic Tuning," *ACS Nano* **10**, 1788–1794 (2016).
 50. K. J. Palm, J. B. Murray, T. C. Narayan, and J. N. Munday, "Dynamic Optical Properties of Metal Hydrides," *ACS Photonics* **5**, 4677–4686 (2018).
 51. K. Tajima, Y. Yamada, S. Bao, M. Okada, and K. Yoshimura, "Flexible all-solid-state switchable mirror on plastic sheet," *Appl. Phys. Lett.* **92**, 041912 (2008).
 52. J. Li, S. Kamin, G. Zheng, F. Neubrech, S. Zhang, and N. Liu, "Addressable metasurfaces for dynamic holography and optical information encryption," *Sci. Adv.* **4**, eaar6768 (2018).
 53. X. Duan and N. Liu, "Magnesium for Dynamic Nanoplasmonics," *Acc. Chem. Res.* **52**, 1979–1989 (2019).
 54. W. Yang, S. Xiao, Q. Song, Y. Liu, Y. Wu, S. Wang, J. Yu, J. Han, and D. P. Tsai, "All-dielectric metasurface for high-performance structural color," *Nat. Commun.* **11**, 1864 (2020).
 55. J. Li, P. Yu, S. Zhang, and N. Liu, "A Reusable Metasurface Template," *Nano Lett.* **20**, 6845–6851 (2020).
 56. J. Hu, D. Wang, D. Bhowmik, T. Liu, S. Deng, M. P. Knudson, X. Ao, and T. W. Odom, "Lattice-Resonance Metalenses for Fully Reconfigurable Imaging," *ACS Nano* **13**, 4613–4620 (2019).
 57. J. Lu, B. Sain, P. Georgi, M. Protte, T. Bartley, T. Zentgraf, J. Lu, B. Sain, P. Georgi, M. Protte, T. Bartley, and T. Zentgraf, "A Versatile Metasurface Enabling Superwettability for Self-Cleaning and Dynamic Color Response," *Adv. Opt. Mater.* **10**, 2101781 (2022).
 58. L. Bi, J. Hu, P. Jiang, H. S. Kim, D. H. Kim, M. C. Onbasli, G. F. Dionne, C. A. Ross, L. Bi, J. Hu, P. Jiang, H. S. Kim, D. H. Kim, M. C. Onbasli, G. F. Dionne, and C. A. Ross, "Magneto-Optical Thin Films for On-Chip Monolithic Integration of Non-Reciprocal Photonic Devices," *Materials* **6**, 5094–5117 (2013).
 59. A. Kazlou, A. L. Chekhov, A. I. Stognij, I. Razdolski, and A. Stupakiewicz, "Surface Plasmon-Enhanced Photomagnetic Excitation of Spin Dynamics in Au/YIG:Co Magneto-Plasmonic Crystals," *ACS Photonics* **8**, 2197–2202 (2021).
 60. M. Ren, B. Jia, J.-Y. Ou, E. Plum, J. Zhang, K. F. MacDonald, A. E. Nikolaenko, J. Xu, M. Gu, and N. I. Zheludev, "Nanostructured Plasmonic Medium for Terahertz Bandwidth All-Optical Switching," *Adv. Mater.* **23**, 5540–5544 (2011).
 61. M. R. Shcherbakov, S. Liu, V. V. Zubyuk, A. Vaskin, P. P. Vabishchevich, G. Keeler, T. Pertsch, T. V. Dolgova, I. Staude, I. Brener, and A. A. Fedyanin, "Ultrafast all-optical tuning of direct-gap semiconductor metasurfaces," *Nat. Commun.* **8**, 17 (2017).
 62. Y. Wu, L. Kang, H. Bao, and D. H. Werner, "Exploiting Topological Properties of Mie-Resonance-Based Hybrid Metasurfaces for Ultrafast Switching of Light Polarization," *ACS Photonics* **7**, 2362–2373 (2020).
 63. O. Quevedo-Teruel, H. Chen, A. Díaz-Rubio, G. Gok, A. Grbic, G. Minatti, E. Martini, S. Maci, G. V. Eleftheriades, M. Chen, N. I. Zheludev, N. Papasimakis, S. Choudhury, Z. A.

- Kudyshev, S. Saha, H. Reddy, A. Boltasseva, V. M. Shalaev, A. V. Kildishev, D. Sievenpiper, C. Caloz, A. Al, Q. He, L. Zhou, G. Valerio, E. Rajo-Iglesias, Z. Sipus, F. Mesa, R. Rodríguez-Berral, F. Medina, V. Asadchy, S. Tretyakov, and C. Craeye, "Roadmap on metasurfaces," *J. Opt.* **21**, 073002 (2019).
64. E. Mikheeva, C. Kyrou, F. Bentata, S. Khadir, S. Cuff, and P. Genevet, "Space and Time Modulations of Light with Metasurfaces: Recent Progress and Future Prospects," *ACS Photonics* **13**, (2022).
 65. T. Badloe, J. Lee, J. Seong, and J. Rho, "Tunable Metasurfaces: The Path to Fully Active Nanophotonics," *Adv. Photonics Res.* **2**, 2000205 (2021).
 66. Y. Che, X. Wang, Q. Song, Y. Zhu, and S. Xiao, "Tunable optical metasurfaces enabled by multiple modulation mechanisms," *Nanophotonics* **9**, 4407–4431 (2020).
 67. J. Yang, S. Gurung, S. Bej, P. Ni, and H. W. Howard Lee, "Active optical metasurfaces: comprehensive review on physics, mechanisms, and prospective applications," *Reports Prog. Phys.* **85**, 036101 (2022).
 68. S. C. Malek, A. C. Overvig, S. Shrestha, and N. Yu, "Active nonlocal metasurfaces," *Nanophotonics* **10**, 655–665 (2021).
 69. A. Li, S. Singh, and D. Sievenpiper, "Metasurfaces and their applications," *Nanophotonics* **7**, 989–1011 (2018).
 70. A. M. Shaltout, V. M. Shalaev, and M. L. Brongersma, "Spatiotemporal light control with active metasurfaces," *Science* **364**, eaat3100 (2019).
 71. C. U. Hail, A. U. Michel, D. Poulikakos, and H. Eghlidi, "Optical Metasurfaces: Evolving from Passive to Adaptive," *Adv. Opt. Mater.* **7**, 1801786 (2019).
 72. M. Y. Shalaginov, S. D. Campbell, S. An, Y. Zhang, C. Ríos, E. B. Whiting, Y. Wu, L. Kang, B. Zheng, C. Fowler, H. Zhang, D. H. Werner, J. Hu, and T. Gu, "Design for quality: reconfigurable flat optics based on active metasurfaces," *Nanophotonics* **9**, 3505–3534 (2020).
 73. Q. He, S. Sun, and L. Zhou, "Tunable/Reconfigurable Metasurfaces: Physics and Applications," *Research* **2019**, 1–16 (2019).
 74. L. Kang, R. P. Jenkins, and D. H. Werner, "Recent Progress in Active Optical Metasurfaces," *Adv. Opt. Mater.* 1801813 (2019).
 75. A. Nemati, Q. Wang, M. Hong, and J. Teng, "Tunable and reconfigurable metasurfaces and metadevices," *Opto-Electronic Adv.* **1**, 18000901–18000925 (2018).
 76. H.-T. Chen, A. J. Taylor, and N. Yu, "A review of metasurfaces: physics and applications," *Reports Prog. Phys.* **79**, 076401 (2016).
 77. T. Cui, B. Bai, and H. B. Sun, "Tunable Metasurfaces Based on Active Materials," *Adv. Funct. Mater.* **29**, 1806692 (2019).
 78. M. N. Julian, C. Williams, S. Borg, S. Bartram, and H. J. Kim, "Reversible optical tuning of GeSbTe phase-change metasurface spectral filters for mid-wave infrared imaging," *Optica* **7**, 746–754 (2020).
 79. C. Williams, N. Hong, M. Julian, S. Borg, and H. J. Kim, "Tunable mid-wave infrared Fabry-Perot bandpass filters using phase-change GeSbTe," *Opt. Express* **28**, 10583 (2020).
 80. A. Sarangan, K. Hirakawa, and R. Heenkenda, "Tunable optical filter using phase change materials for smart IR night vision applications," *Opt. Express* **29**, 33795–33803 (2021).
 81. S. Q. Li, X. Xu, R. M. Veetil, V. Valuckas, R. Paniagua-Domínguez, and A. I. Kuznetsov, "Phase-only transmissive spatial light modulator based on tunable dielectric metasurface," *Science* **364**, 1087–1090 (2019).

82. J. Park, B. G. Jeong, S. Il Kim, D. Lee, J. Kim, C. Shin, C. B. Lee, T. Otsuka, J. Kyoung, S. Kim, K. Y. Yang, Y. Y. Park, J. Lee, I. Hwang, J. Jang, S. H. Song, M. L. Brongersma, K. Ha, S. W. Hwang, H. Choo, and B. L. Choi, "All-solid-state spatial light modulator with independent phase and amplitude control for three-dimensional LiDAR applications," *Nat. Nanotechnol.* **16**, 69–76 (2020).
83. J. Hua, W. Qiao, and L. Chen, "Recent Advances in Planar Optics-Based Glasses-Free 3D Displays," *Front. Nanotechnol.* **4**, 829011 (2022).
84. D. Fattal, Z. Peng, T. Tran, S. Vo, M. Fiorentino, J. Brug, and R. G. Beausoleil, "A multi-directional backlight for a wide-angle, glasses-free three-dimensional display," *Nature* **495**, 348–351 (2013).
85. D. Wen, J. J. Cadusch, J. Meng, and K. B. Crozier, "Light field on a chip: metasurface-based multicolor holograms," *Adv. Photonics* **3**, 024001 (2021).
86. G. Arya, W. F. Li, C. Roques-Carmes, M. Soljačić, S. G. Johnson, and Z. Lin, "End-to-End Optimization of Metasurfaces for Imaging with Compressed Sensing," *arXiv:2201.12348* (2022).
87. T. Zhou, X. Lin, J. Wu, Y. Chen, H. Xie, Y. Li, J. Fan, H. Wu, L. Fang, and Q. Dai, "Large-scale neuromorphic optoelectronic computing with a reconfigurable diffractive processing unit," *Nat. Photonics* **15**, 367–373 (2021).
88. T. Zhou, T. Zhou, T. Zhou, L. Fang, L. Fang, T. Yan, T. Yan, J. Wu, J. Wu, Y. Li, Y. Li, J. Fan, J. Fan, H. Wu, H. Wu, X. Lin, X. Lin, X. Lin, X. Lin, Q. Dai, Q. Dai, Q. Dai, and Q. Dai, "In situ optical backpropagation training of diffractive optical neural networks," *Photonics Res.* **8**, 940–953 (2020).
89. L. Huang, S. Zhang, and T. Zentgraf, "Metasurface holography: From fundamentals to applications," *Nanophotonics* **7**, 1169–1190 (2018).
90. J. Li, P. Yu, S. Zhang, and N. Liu, "Electrically-controlled digital metasurface device for light projection displays," *Nat. Commun.* **11**, 3574 (2020).
91. H. Gao, X. Fan, W. Xiong, M. Hong, H. Gao, X. Fan, W. Xiong, and M. Hong, "Recent advances in optical dynamic meta-holography," *Opto-Electronic Adv.* **4**, 210030- (2021).
92. S. G. Carrillo, L. Trimby, Y. Au, V. K. Nagareddy, G. Rodriguez-Hernandez, P. Hosseini, C. Ríos, H. Bhaskaran, and C. D. Wright, "A Nonvolatile Phase-Change Metamaterial Color Display," *Adv. Opt. Mater.* **7**, 1801782 (2019).
93. H. Liu, H. Yang, Y. Li, B. Song, Y. Wang, Z. Liu, L. Peng, H. Lim, J. Yoon, W. Wu, H. Liu, H. Yang, Y. Li, B. Song, Y. Wang, Z. Liu, W. Wu Ming Hsieh, L. Peng Futurewei, H. Lim, and J. Yoon, "Switchable All-Dielectric Metasurfaces for Full-Color Reflective Display," *Adv. Opt. Mater.* **7**, 1801639 (2019).
94. O. Hemmatyar, S. Abdollahramezani, I. Zeimpekis, S. Lepeshov, A. Krasnok, A. I. Khan, K. M. Neilson, C. Teichrib, T. Brown, E. Pop, D. W. Hewak, M. Wuttig, A. Alu, O. L. Muskens, and A. Adibi, "Enhanced Meta-Displays Using Advanced Phase-Change Materials," *arXiv:2107.12159* (2021).
95. F. Yang, H.-I. Lin, M. Y. Shalaginov, K. Stoll, S. An, C. Rivero-Baleine, M. Kang, A. Agarwal, K. Richardson, H. Zhang, J. Hu, and T. Gu, "Reconfigurable parafocal zoom metalens," *Adv. Opt. Mater.* (2022).
96. J. Zhang, Y. Kosugi, A. Otomo, Y.-L. L. Ho, J.-J. J. Delaunay, Y. Nakano, and T. Tanemura, "Electrical tuning of metal-insulator-metal metasurface with electro-optic polymer," *Appl. Phys. Lett.* **113**, 231102 (2018).
97. A. Otomo, J. Zhang, T. Tanemura, Y. Nakano, and Y. Kosugi, "Active metasurface

- modulator with electro-optic polymer using bimodal plasmonic resonance," *Opt. Express* **25**, 30304–30311 (2017).
98. A. She, S. Zhang, S. Shian, D. R. Clarke, and F. Capasso, "Adaptive metalenses with simultaneous electrical control of focal length, astigmatism, and shift," *Sci. Adv.* **4**, eaap9957 (2018).
 99. R. J. Zawadzki, S. M. Jones, S. ; R. J. Zawadzki, . Y Zhang, J. S. Rha, R. Jonnal, and D. Miller, "High-speed adaptive optics for imaging of the living human eye," *Opt. Express* **23**, 23035–23052 (2015).
 100. X. Guo, Y. Ding, Y. Duan, and X. Ni, "Nonreciprocal metasurface with space–time phase modulation," *Light Sci. Appl.* **8**, 123 (2019).
 101. X. Wang, A. Díaz-Rubio, H. Li, S. A. Tretyakov, and A. Alù, "Theory and Design of Multifunctional Space-Time Metasurfaces," *Phys. Rev. Appl.* **13**, 044040 (2020).
 102. L. Zhang and T. J. Cui, "Space-Time-Coding Digital Metasurfaces: Principles and Applications," *Research* **2021**, 9802673 (2021).
 103. A. Howes, Z. Zhu, D. Curie, J. R. Avila, V. D. Wheeler, R. F. Haglund, and J. G. Valentine, "Optical Limiting Based on Huygens' Metasurfaces," *Nano Lett.* **20**, 4638–4644 (2020).
 104. S. A. Mann, N. Nookala, S. Johnson, A. Mekki, J. F. Klem, I. Brener, M. Raschke, A. Alu, and M. A. Belkin, "Ultrafast optical switching and power limiting in intersubband polaritonic metasurfaces," *Optica* **8**, 606–613 (2021).
 105. Y. Liu, J. Song, W. Zhao, X. Ren, Q. Cheng, X. Luo, N. X. Fang, and R. Hu, "Dynamic thermal camouflage via a liquid-crystal-based radiative metasurface," *Nanophotonics* **9**, 855–863 (2020).
 106. Y. Qu, Q. Li, L. Cai, M. Pan, P. Ghosh, K. Du, and M. Qiu, "Thermal camouflage based on the phase-changing material GST," *Light Sci. Appl.* **7**, 26 (2018).
 107. F. Yang, F. Yang, S. An, M. Y. Shalaginov, H. Zhang, C. Rivero-Baleine, J. Hu, J. Hu, T. Gu, and T. Gu, "Design of broadband and wide-field-of-view metalenses," *Opt. Lett.* **46**, 5735–5738 (2021).
 108. F. Yang, S. An, M. Y. Shalaginov, H. Zhang, J. Hu, and T. Gu, "Wide field-of-view flat lens: an analytical formalism," *arXiv:2108.09295* (2021).
 109. S. Banerji, M. Meem, A. Majumder, B. Sensale-Rodriguez, and R. Menon, "Extreme-depth-of-focus imaging with a flat lens," *Optica* **7**, 214 (2020).
 110. P. Wang, N. Mohammad, and R. Menon, "Chromatic-aberration-corrected diffractive lenses for ultra-broadband focusing," *Sci. Rep.* **6**, 21545 (2016).
 111. M. Meem, A. Majumder, S. Banerji, J. C. Garcia, O. B. Kigner, P. W. C. Hon, B. Sensale-Rodriguez, and R. Menon, "Imaging from the visible to the longwave infrared wavelengths via an inverse-designed flat lens," *Opt. Express* **29**, 20715 (2021).
 112. Z. Li, P. Lin, Y. W. Huang, J. S. Park, W. T. Chen, Z. Shi, C. W. Qiu, J. X. Cheng, and F. Capasso, "Meta-optics achieves RGB-achromatic focusing for virtual reality," *Sci. Adv.* **7**, 4458–4485 (2021).
 113. H. Zhang, L. Zhou, L. Lu, J. Xu, N. Wang, H. Hu, B. M. A. Rahman, Z. Zhou, and J. Chen, "Miniature Multilevel Optical Memristive Switch Using Phase Change Material," *ACS Photonics* **6**, 2205–2212 (2019).
 114. J. Zheng, Z. Fang, C. Wu, S. Zhu, P. Xu, J. K. Doylend, S. Deshmukh, E. Pop, S. Dunham, M. Li, and A. Majumdar, "Nonvolatile Electrically Reconfigurable Integrated Photonic Switch Enabled by a Silicon PIN Diode Heater," *Adv. Mater.* **32**, 2001218 (2020).
 115. H. Zhang, L. Zhou, J. Xu, N. Wang, H. Hu, L. Lu, B. M. A. Rahman, and J. Chen,

- "Nonvolatile waveguide transmission tuning with electrically-driven ultra-small GST phase-change material," *Sci. Bull.* **64**, 782–789 (2019).
116. K. Kato, M. Kuwahara, H. Kawashima, T. Tsuruoka, and H. Tsuda, "Current-driven phase-change optical gate switch using indium–tin-oxide heater," *Appl. Phys. Express* **10**, 072201 (2017).
 117. C. Wu, H. Yu, H. Li, X. Zhang, I. Takeuchi, and M. Li, "Low-Loss Integrated Photonic Switch Using Subwavelength Patterned Phase Change Material," *ACS Photonics* **6**, 87–92 (2018).
 118. A. Gallmon, A. Adibi, A. E. Dorche, A. A. Eftekhari, A. H. Hosseinnia, H. Taghinejad, O. Hemmatyar, S. Abdollahramezani, T. Fan, A. E. Dorche, A. Gallmon, and A. Adibi, "ITO-based microheaters for reversible multi-stage switching of phase-change materials: towards miniaturized beyond-binary reconfigurable integrated photonics," *Opt. Express* **29**, 20449–20462 (2021).
 119. C. Ríos, Y. Zhang, M. Y. Shalaginov, S. Deckoff-Jones, H. Wang, S. An, H. Zhang, M. Kang, K. A. Richardson, C. Roberts, J. B. Chou, V. Liberman, S. A. Vitale, J. Kong, T. Gu, and J. Hu, "Multi-Level Electro-Thermal Switching of Optical Phase-Change Materials Using Graphene," *Adv. Photonics Res.* **2**, 2000034 (2020).
 120. J. Zheng, S. Zhu, P. Xu, S. Dunham, and A. Majumdar, "Modeling Electrical Switching of Nonvolatile Phase-Change Integrated Nanophotonic Structures with Graphene Heaters," *ACS Appl. Mater. Interfaces* **12**, 21827–21836 (2020).
 121. Y. Zhang, J. Li, J. Chou, Z. Fang, A. Yadav, H. Lin, Q. Du, J. Michon, Z. Han, Y. Huang, H. Zheng, T. Gu, V. Liberman, K. Richardson, and J. Hu, "Broadband Transparent Optical Phase Change Materials," in *Conference on Lasers and Electro-Optics* (OSA, 2017), p. JTh5C.4.
 122. Q. Zhang, Y. Zhang, J. Li, R. Soref, T. Gu, and J. Hu, "Broadband nonvolatile photonic switching based on optical phase change materials: beyond the classical figure-of-merit," *Opt. Lett.* **43**, 94–97 (2018).
 123. S. An, C. Fowler, B. Zheng, M. Y. Shalaginov, H. Tang, H. Li, L. Zhou, J. Ding, A. M. Agarwal, C. Rivero-Baleine, K. A. Richardson, T. Gu, J. Hu, and H. Zhang, "A Deep Learning Approach for Objective-Driven All-Dielectric Metasurface Design," *ACS Photonics* **6**, 3196–3207 (2019).
 124. J. Park, S. J. Kim, V. J. Sorger, and S. J. Kim, "Electrically tunable metasurface by using InAs in a metal-insulator-metal configuration," *Nanophotonics* **11**, 1117–1126 (2022).
 125. H. Madan, H.-T. Zhang, M. Jerry, D. Mukherjee, N. Alem, R. Engel-Herbert, and S. Datta, "26.5 Terahertz electrically triggered RF switch on epitaxial VO₂-on-Sapphire (VOS) wafer," in *2015 IEEE International Electron Devices Meeting (IEDM)* (IEEE, 2015), pp. 9.3.1–9.3.4.
 126. M. F. Jager, C. Ott, P. M. Kraus, C. J. Kaplan, W. Pouse, R. E. Marvel, R. F. Haglund, D. M. Neumark, and S. R. Leone, "Tracking the insulator-to-metal phase transition in VO₂ with few-femtosecond extreme UV transient absorption spectroscopy," *Proc. Natl. Acad. Sci. U. S. A.* **114**, 9558–9563 (2017).
 127. S. Cuffey, J. John, Z. Zhang, J. Parra, J. Sun, R. Orobtcouk, S. Ramanathan, and P. Sanchis, "VO₂ nanophotonics," *APL Photonics* **5**, 110901 (2020).
 128. K. Dong, S. Hong, Y. Deng, H. Ma, J. Li, X. Wang, J. Yeo, L. Wang, S. Lou, K. B. Tom, K. Liu, Z. You, Y. Wei, C. P. Grigoropoulos, J. Yao, and J. Wu, "A Lithography-Free and Field-Programmable Photonic Metacanvas," *Adv. Mater.* **30**, 1703878 (2018).

129. W. Kim, M. Brightsky, T. Masuda, N. Sosa, S. Kim, R. Bruce, F. Carta, G. Fraczak, H. Y. Cheng, A. Ray, Y. Zhu, H. L. Lung, K. Suu, and C. Lam, "ALD-based confined PCM with a metallic liner toward unlimited endurance," in *Technical Digest - International Electron Devices Meeting, IEDM* (Institute of Electrical and Electronics Engineers Inc., 2017), pp. 4.2.1-4.2.4.
130. N. Youngblood, C. Ríos, E. Gemo, J. Feldmann, Z. Cheng, A. Baldycheva, W. H. Pernice, C. David Wright, H. Bhaskaran, N. Youngblood, C. Ríos, Z. Cheng, H. Bhaskaran, E. Gemo, A. Baldycheva, C. D. Wright, J. Feldmann, and W. H. P Pernice, "Tunable Volatility of Ge₂Sb₂Te₅ in Integrated Photonics," *Adv. Funct. Mater.* **29**, 1807571 (2019).
131. J. C. Lacroix, K. K. Kanazawa, and A. Diaz, "Polyaniline: A Very Fast Electrochromic Material," *J. Electrochem. Soc.* **136**, 1308–1313 (1989).
132. H. T. Zhang, T. J. Park, A. N. M. N. Islam, D. S. J. Tran, S. Manna, Q. Wang, S. Mondal, H. Yu, S. Banik, S. Cheng, H. Zhou, S. Gamage, S. Mahapatra, Y. Zhu, Y. Abate, N. Jiang, S. K. R. S. Sankaranarayanan, A. Sengupta, C. Teuscher, and S. Ramanathan, "Reconfigurable perovskite nickelate electronics for artificial intelligence," *Science* **375**, 533–539 (2022).
133. C. J. Barile, D. J. Slotcavage, J. Hou, M. T. Strand, T. S. Hernandez, and M. D. McGehee, "Dynamic Windows with Neutral Color, High Contrast, and Excellent Durability Using Reversible Metal Electrodeposition," *Joule* **1**, 133–145 (2017).
134. P. Pintus, L. Ranzani, S. Pinna, D. Huang, M. V. Gustafsson, F. Karinou, G. A. Casula, Y. Shoji, Y. Takamura, T. Mizumoto, M. Soltani, and J. E. Bowers, "A low-power integrated magneto-optic modulator on silicon for cryogenic applications," *arXiv:2109.04538* (2021).
135. I. Moreno, C. Iemmi, A. Márquez, J. Campos, and M. J. Yzuel, "Modulation light efficiency of diffractive lenses displayed in a restricted phase-mostly modulation display," *Appl. Opt.* **43**, 6278–6284 (2004).
136. P. Thureja, G. K. Shirmanesh, K. T. Fountaine, R. Sokhoyan, M. Grajower, and H. A. Atwater, "Array-level inverse design of beam steering active metasurfaces," *ACS Nano* **14**, 15042–15055 (2020).
137. C. H. Liu, J. Zheng, S. Colburn, T. K. Fryett, Y. Chen, X. Xu, and A. Majumdar, "Ultrathin van der Waals Metalenses," *Nano Lett.* **18**, 6961–6966 (2018).